This manuscript is a ***preprint*** submitted for review to *PALAIOS* and has not been peer-reviewed.

September 12, 2024

SEDIMENTOLOGICAL CONTROLS ON PLANT-FOSSIL PRESERVATION IN AN EOCENE CALDERA-LAKE FILL: A HIGH-RESOLUTION, AGE-CONSTRAINED RECORD FROM THE TUFOLITAS LAGUNA DEL HUNCO, CHUBUT PROVINCE, ARGENTINA

ELIZABETH A. HAJEK[1]*, J. MARCELO KRAUSE[2,3], PETER WILF[1], MARK D. SCHMITZ[4]
[1]Department of Geosciences, Pennsylvania State University, USA
[2]CONICET-Museo Paleontológico Egidio Feruglio, Argentina
[3]Universidad Nacional de Río Negro, Argentina
[4]Department of Geosciences, Boise State University, USA

*Corresponding Author: hajek@psu.edu

SEDIMENTOLOGICAL CONTROLS ON PLANT-FOSSIL PRESERVATION IN AN EOCENE CALDERA-LAKE FILL: A HIGH-RESOLUTION, AGE-CONSTRAINED RECORD FROM THE TUFOLITAS LAGUNA DEL HUNCO, CHUBUT PROVINCE, ARGENTINA

ELIZABETH A. HAJEK[1*], J. MARCELO KRAUSE[2,3], PETER WILF[1], MARK D. SCHMITZ[4]
[1]Department of Geosciences, Pennsylvania State University, University Park, Pennsylvania 16802 USA
[2]CONICET-Museo Paleontológico Egidio Feruglio, Av. Fontana 140, 9100 Trelew, Chubut, Argentina
[3]Universidad Nacional de Río Negro, Av. Roca 1422, 8332 General Roca, Río Negro, Argentina
[4]Department of Geosciences, Boise State University, 1910 University Drive, Boise, Idaho 83725, USA
[*]Corresponding Author; hajek@psu.edu

ABSTRACT

Caldera lake sediments of the early Eocene Tufolitas Laguna del Hunco (Chubut Province, Argentina) host one of the world's best-preserved and most diverse fossil plant assemblages, but the exceptional quality of preservation remains unexplained. The fossils have singular importance because they include numerous oldest and unique occurrences in South America of genera that today are restricted to the West Pacific region, where many of them are now vulnerable to extinction. Lacustrine depositional settings are often considered optimal for preservation as passive receptors of suspended sediment delivered, often seasonally, from lakeshores. However, caldera lakes can be influenced by a broader range of physical and chemical processes that enhance or decrease fossil preservation potential. Here, we use Laguna del Hunco to provide a new perspective on paleoenvironmental controls on plant fossil preservation in tectonically active settings. We establish a refined geochronological framework for the Laguna del Hunco deposits and present a detailed history of processes active during ~200,000 years of lake filling from 52.217 ± 0.014 Ma to 51.988 ± 0.35 Ma, the time interval that encompasses nearly all fossil deposition. Detailed facies analysis shows that productive fossil localities reside within high-deposition-rate beds associated with high-energy density flows and wave-reworked lake-floor sediments, challenging traditional views that low-energy environments are required for well-preserved plant fossils. These results demonstrate that even delicate fossil components like fruits and flowers can survive high-energy transport, underscoring the importance of rapid burial as a primary control on fossil preservation. Short, steep sediment-transport networks may facilitate terrestrial fossil preservation by limiting opportunities for biochemical degradation on land and providing relatively frequent, high-energy depositional events, which quickly transport and bury organic material following events such as landslides from steep, wet, surrounding slopes. Our new model for plant taphonomy opens a path toward finding and understanding other exceptional biotas in environments once considered unlikely for preservation.

INTRODUCTION

Detailed sedimentological reconstructions provide important perspectives on the tectonic and climatic history of a region and insight into controls on fossil preservation, helping to assess sampling and preservation biases and determine what parts of an ancient ecosystem are reflected in a particular fossil assemblage. Deposits of the early Eocene Tufolitas Laguna del Hunco at Laguna del Hunco, Chubut Province, Argentina (Figure 1) offer a unique, high-resolution snapshot of late-Gondwanan rainforests and the paleoecology and paleogeography of the Southern Hemisphere. The Laguna del Hunco deposits host a world-class, highly diverse fossil assemblage that has provided key data constraining how Gondwanan plant lineages – for which many living relative genera now inhabit West Pacific tropical rainforests – evolved and migrated in relation to the southern super-continent's breakup (e.g., Romero & Hickey, 1976; Romero, 1986; Wilf *et al.*, 2003, 2013, 2017, 2019, 2023; Zamaloa *et al.*, 2006, 2020; Gandolfo *et al.*, 2011; Kooyman *et al.*, 2014; Deanna *et al.*, 2020; Matel *et al.*, 2022). The flora is renowned for its extremely delicate plant reproductive structures such as flowers, fruits, and whole infructescences, and no explanation has previously emerged for this exceptional preservation.

Lacustrine settings generally comprise favorable conditions for fossil preservation (e.g., MacGinitie, 1953; Smith, 2012), and relatively low hydrodynamic energy in these systems facilitates preservation of delicate organs. Caldera lakes offer an opportunity to explore high-energy extremes in lacustrine settings. For example, large airfall events can abruptly blanket a lake with sediment (e.g., Anderson *et al.*, 1984); local tectonism and vulcanism can violently shake the lake and its surrounding hillslopes; and landslides and slumps from steep caldera margins can rapidly deliver pulses of sediment to a lake basin and generate waves that interact with the lake bed (e.g., Couston *et al.*, 2015). Additionally, chemistry associated with volcanic eruptions and sub-surface volatile fluxes can create conditions that either favor or inhibit the preservation of organic matter (e.g., Varekamp, 2015). Consequently, tectonically active settings like Laguna del Hunco provide important end-member constraints for the controls on fossil burial and preservation in lacustrine settings.

Here, we present new results that provide high-resolution age constraints on the Laguna del Hunco biota and a detailed facies analysis that refines understanding about the sedimentary processes that control paleofloral preservation in tectonically active lake settings. Our observations indicate that the lake experienced overall balanced fill and a long-term decrease in local, active tectonism coincident with an increase in blanketing airfall events. The exceptional fossil plant preservation occurred in facies associated with high-energy, high-deposition-rate events like episodic density flows and lake-bed wave reworking. Observations from Laguna del Hunco highlight the potential for delicate plant material like flowers and fruits to be moved through vigorous sediment-transport processes and preserved intact when transport networks are short and sedimentation rates are high.

STUDY AREA

The Laguna del Hunco locality in Chubut province, Argentina (Figure 1) hosts a remarkably well-preserved and diverse early Eocene biotic assemblage (Figure 2) and offers an important window into Southern-Hemisphere floristic composition, paleobiogeography, and paleoecology during the latest stages of Gondwana. Paleontological studies of fossil plants, insects, and vertebrates from Laguna del Hunco began in the 1920s (e.g., Berry, 1925; Dolgopol de Sáez, 1941; Casamiquela, 1961; Romero & Hickey, 1976; Fidalgo & Smith, 1987) and have accelerated through intensive collection and study over the past 25 years. Some notable recent discoveries from the fossil flora of over 200 species, among many examples (Wilf *et al.*, 2013, 2019; Barreda *et al.*, 2020), include the oldest and first non-Australian *Eucalyptus* fossils (Gandolfo *et al.*, 2011; Zamaloa *et al.*, 2020); the first Western Hemisphere fossils of the giant West Pacific kauri conifer, *Agathis* (Wilf *et al.*, 2014); the first Southern Hemisphere fossils of the beech family Fagaceae, assigned to the Asian chinkapin genus *Castanopsis* (Wilf *et al.*, 2019); and the first fossil fruits and oldest fossils of the nightshade family Solanaceae, assigned to the living tomatillo genus *Physalis* (Wilf *et al.*, 2017; Deanna *et al.*, 2020).

Most of the fossil plants from Laguna del Hunco are compressions of diverse foliage and reproductive structures (Wilf *et al.*, 2003, 2005), but silicified tree ferns, conifers, and angiosperms are recently reported, along with a rich palynoflora from scarce organic-rich horizons (Bomfleur & Escapa, 2019; Barreda *et al.*, 2020; Pujana *et al.*, 2020; Brea *et al.*, 2021). These invaluable specimens are preserved within caldera lake sediments (e.g., Petersen, 1946; Aragón & Romero, 1984; Wilf *et al.*, 2003; Gosses *et al.*, 2021) known as the Tufolitas Laguna del Hunco, part of the Eocene Huitrera Formation (Aragón & Mazzoni, 1997; Aguilera *et al.*, 2018; Aragón *et al.*, 2018).

The Tufolitas are part of the Middle Chubut River Pyroclastic and Volcanic Complex and are exposed throughout the Piedra Parada caldera system, which formed during an Eocene volcanic flare-up associated with the Farallon-Aluk slab window opening beneath the southern Cordillera around 52 million years ago (Aragón *et al.*, 2018). Exceptional fossil preservation occurs abundantly in the study area (Figure 1) next to the small modern playa known locally as Laguna del Hunco (LH; "lake of rushes"), for which the fossil site is named.

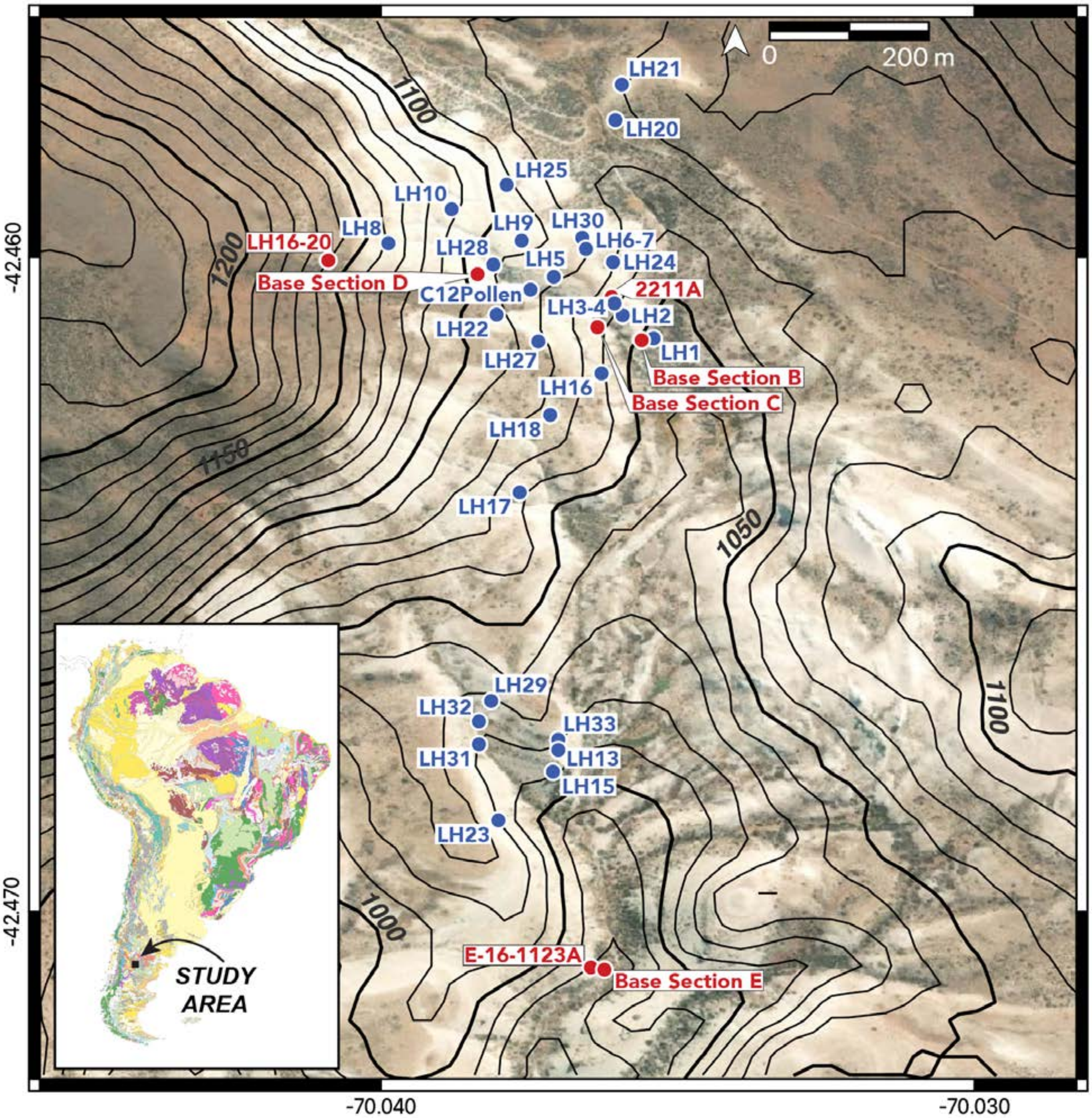

FIGURE 1: Study area map with satellite photo (ESRI) and elevation contours (in meters). Fossil localities are shown in blue, and U-Pb geochronology localities and the magnetostratigraphic section bases of Wilf et al. (2003) are shown in red. Locality LH26 lies ~1 km northwest of LH21 (Supplement). Inset shows Geologic Map of South American Geology (Gómez *et al.*, 2019).

Gosses et al. (2021) provided an updated regional overview of the Piedra Parada caldera fill, including a series of new ^{40}Ar-^{39}Ar dates that, along with previously published ^{40}Ar-^{39}Ar ages and paleomagnetic stratigraphy (Wilf *et al.*, 2003, 2005), helped constrain the relative ages of lacustrine deposits within the succession. The caldera is >40 km in its longest (north-south) dimension and is underlain by a large ignimbrite unit that formed the caldera floor, the Ignimbrita Barda Colorada (IBC; Mazzoni *et al.*, 1989); the uppermost beds of the IBC yielded an ^{40}Ar-^{39}Ar age of 52.54 ± 0.17 Ma (Gosses *et al.*, 2021), setting a maximum depositional age for the overlying fossil lake beds. At Laguna del Hunco, the Tufolitas Laguna del Hunco comprise a ~200 m-thick succession of tuffaceous, fossiliferous lake sediments that filled the caldera basin containing interspersed basalts and ignimbrite deposits. A set of three ^{40}Ar-^{39}Ar dates from primary tuffs and ash-rich sediments in the Tufolitas LH analyzed by the late John Obradovich (in Wilf *et al.*, 2003) all yielded early Eocene ages near 52 Ma. Of those, sanidine, considered to produce the most reliable ages, was analyzed only from Ash 2211A (Figure 1), which, after re-analysis and recalibration to modern constants by Michael Smith (in Wilf, 2012) produced the widely cited 52.22 ± 0.22 Ma age for the middle of the densely fossiliferous interval (e.g., Barreda *et al.*, 2020). However, the section has, until now, lacked a reliable radiometric constraint from within the lake beds for the basal and upper levels, limiting temporal precision for the fossils, and the ^{40}Ar-^{39}Ar dates have not been cross-checked with the U-Pb system. The most applicable constraint for the end of lake fill has been the 49.19 ± 0.19 Ma age of the Southern Ignimbrite of Gosses et al. (2021), which sits atop Tufolitas LH exposures in the southern caldera but has not been correlated to the Laguna del Hunco section in the northern caldera. In addition to the prior ^{40}Ar-^{39}Ar work, Jason Hicks (in Wilf et al. 2003) detected six paleomagnetic reversals in 170 m of section of the Tufolitas LH at Laguna del Hunco and correlated the lake beds there to magnetic polarity chrons C23n.2r, C23n.2n, and C23n.1r.

The caldera lake was positioned at ~47-48° S paleolatitude (e.g., Somoza, 2007), and active lake sedimentation took place during the Early Eocene Climatic Optimum (Wilf *et al.*, 2003; Krause *et al.*, 2017), supporting extremely rich floral assemblages whose closest surviving relatives are today associated with everwet rainforest conditions. Caldera margins would most likely have been relatively steep and heavily vegetated, with multistratal rainforests including oak-laurel (*Castanopsis* and Lauraceae) forests with diverse additional angiosperms, similar to those found extensively in lower montane areas of Asia ranging from the eastern Himalayas to New Guinea; diverse and large conifers such as kauris, *Araucaria*, podocarps, and cypresses; extensive areas dominated by *Eucalyptus*, most likely on recent lava flows and landslides; and understory plants and climbers such as tomatillos, supplejacks, moonseeds, *Macaranga*, Rubiaceae, asters, cycads, and diverse ferns (Wilf, 2012; Carvalho *et al.*, 2013; Wilf *et al.*, 2013, 2014, 2019, 2023; Gandolfo & Hermsen, 2017; Jud *et al.*, 2018; Barreda *et al.*, 2020; Rossetto-Harris *et al.*, 2020). Floral assemblages preserved in Laguna del Hunco sediments indicate high biodiversity and establish the extensive former reach of late-Gondwana rainforests and the dispersal of their plant lineages, largely via the later northward movement of Australia and its Neogene collision with Asia that enabled them to reach large areas of Australasia and Southeast Asia (e.g., Kooyman *et al.*, 2014, 2019; Wilf *et al.*, 2019). Today, many of the survivor lineages are under severe threat from rapid land clearance, fire, and climate change (Kooyman *et al.*, 2022).

Within the broader context of the paleogeographic and sedimentary setting of the Piedra Parada caldera (Gosses *et al.*, 2021), we conducted a detailed sedimentological study of the highly fossiliferous Laguna del Hunco local section to understand how process controls on sedimentation in the caldera influenced fossil taphonomy and how that insight may be helpful for reconstructing caldera-rim plant assemblages and controls on exceptional fossil preservation in tectonically active settings. Additionally, we obtained new radiometric dates at the base and top of the fossiliferous interval, bracketing nearly all fossil localities from the local section, and re-analyzed the 2211A ash from the middle of the section to further constrain the specific timing of deposition and refine the chronology of important fossil localities.

Figure 2: Examples of fossil preservation at Laguna del Hunco. A) Various field-trimmed plant fossils from quarry LH2. B) Infructescence of the fossil spurge *Tineafructus casamiquelae* (Euphorbiaceae; Wilf et al. 2023; MPEF-Pb 7989a, quarry LH29), with additional flowers, leaves, and insects. C) *Castaneophyllum patagonicum* leaf (Fagaceae; Wilf et al., 2019; MPEF-Pb 8257, quarry LH13). D) Frond portion of the fern *Todea amissa* (Osmundaceae; Carvalho et al. 2013, quarry LH27). E) Leaf of *Dobineaites ameghinoi* (Anacardiaceae; MPEF-Pb 7839, Wilf, *et al.*, 2024; quarry LH4). F) Frond of the cycad *Austrozamia stockeyae* (Zamiaceae; Wilf et al. 2016; MPEF-Pb 8340, quarry LH27). G) Leafy twig of the yellowwood conifer *Dacrycarpus puertae* (Podocarpaceae; Wilf 2012; MPEF-Pb 973, quarry LH15). (H) Leaf of *Atherospermophyllum guinazui* (Atherospermataceae; Knight and Wilf 2013; MPEF-Pb 5639, quarry LH13). I) Silicified wood, in float. (J) Leaves of an unknown dicot (left) and *Castaneophyllum patagonicum* (right; Fagaceae, field number LH04(2019)-093, quarry LH4). (K) Infructescence with four fruits of the chinkapin *Castanopsis rothwellii* (Fagaceae; Wilf et al., 2019; MPEF-Pb 6433a, quarry LH13). L) Taphocoenosis of disarticulated insect bodies and wings, quarry LH6. M) The pipoid frog *Shelania pascuali* (MPEF-PV 1565; Casamiquela 1961), found in weathered float. N) Lantern fruit of the tomatillo *Physalis infinemundi* (Solanaceae; Wilf et al., 2017; MPEF-Pb 6434a, quarry LH13). (O) *Dacrycarpus puertae*, leafy branch with fleshy podocarpium and two seed cones, MPEF-Pb 4983a, quarry LH13. P) Pollen cone of the monkey-puzzle conifer *Araucaria huncoensis* (Araucariaceae; Rossetto-Harris et al., 2020; MPEF-Pb 10617, quarry LH13). All fossils shown are curated in the Paleontology Collections of the Museo Paleontológico Egidio Feruglio (MPEF-Pb and MPEF-PV), Trelew, Chubut, Argentina.

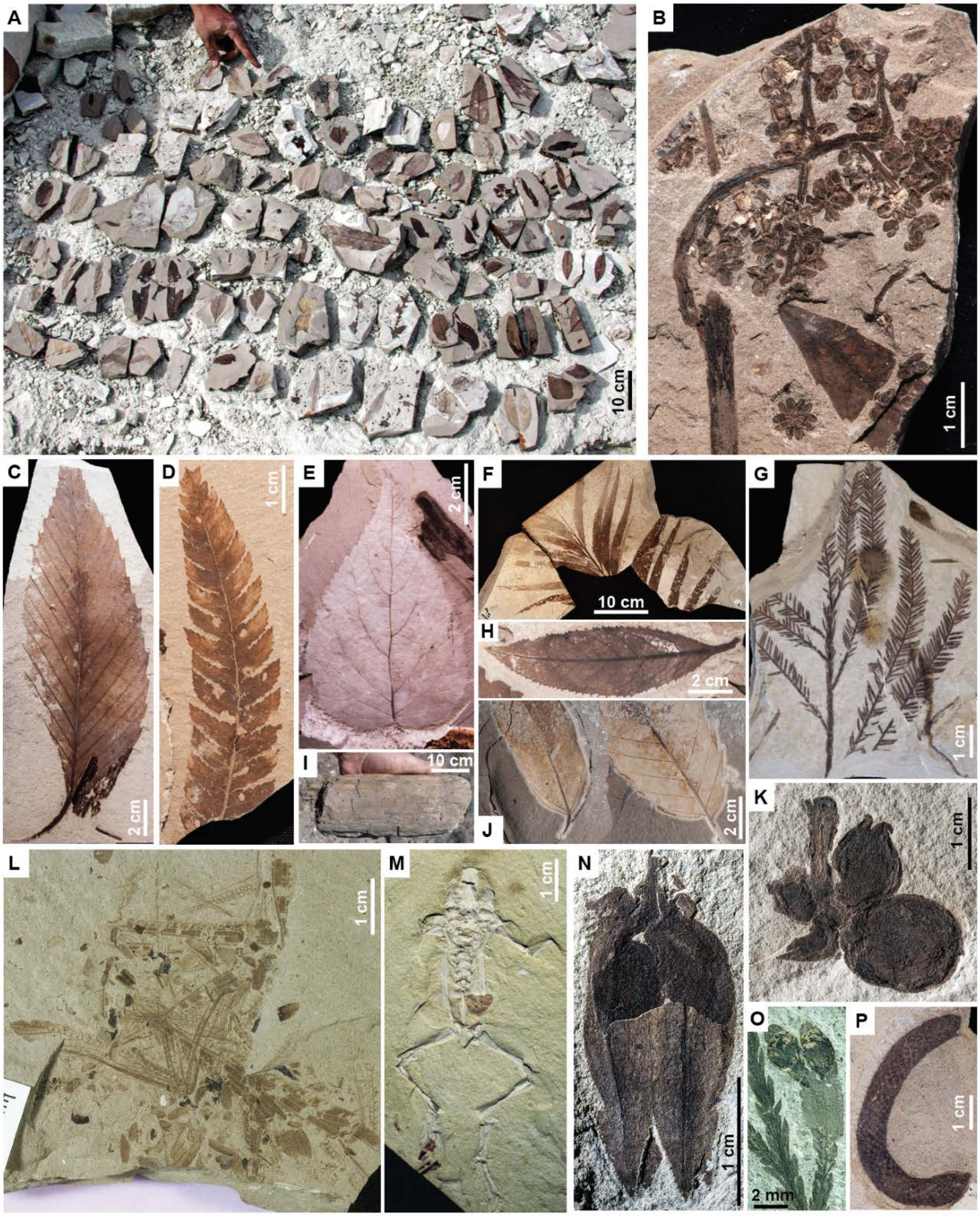
A
10 cm
B
1 cm
C
2 cm
D
1 cm
E
2 cm
F
10 cm
G
1 cm
H
2 cm
I
10 cm
J
2 cm
K
1 cm
L
1 cm
M
1 cm
N
1 cm
O
2 mm
P
1 cm

METHODS

Fieldwork was conducted in 2016 and 2019 and focused on centimeter-scale facies descriptions in the vicinity of fossil localities, along with detailed facies analyses of all lake sediments to reconstruct a sequence-stratigraphic-style interpretation of the caldera lake filling history. Direct field observations followed the measured section from Wilf et al. (2003), used to establish a geochronologic framework for the interval, and were supplemented with drone- and geologist-acquired outcrop photography, which was used to create 3D digital outcrop models of parts of the field area; the models aided in correlation and provided larger-scale stratigraphic context for individual localities.

Primary tuff samples were collected near the bottom and top of the section; we resampled the same bed as the 2311A geochronology sample of Wilf et al., 2003 (E-16-2311A), and sampled a tuff bed near the top of the well-exposed section (LH-16-20; Figures 1 and 3). The samples were analyzed at the Boise State University Isotope Geology Laboratory. Hand samples were separated using conventional density and magnetic methods, and elongate, prismatic zircon crystals (~100-300 microns long) were selected for analysis. Zircon crystals were annealed (following Nasdala *et al.*, 2002; Allen & Campbell, 2012). Individual grains from each sample were selected for U-Pb geochronology analysis using isotope dilution thermal ionization mass spectrometry, following Davydov *et al.* (2010) and Schmitz and Davydov (2012). U-Pb dates and uncertainties for each grain were calculated using algorithms from Schmitz and Schone (2007) and the U decay constants of Jaffey *et al.* (1971); dates are reported with 2-sigma errors. Using the same procedures, a new U-Pb date was obtained by re-analyzing material from Wilf et al. (2003) sample 2211A to provide a more precise age from the middle of the fossiliferous section (Figure 1).

RESULTS

The fossiliferous interval of Laguna del Hunco is bracketed by two new U-Pb ages that constrain the timing of fossil deposition and lake filling from 52.217 ± 0.014 Ma to 51.988 ± 0.035 Ma. The Tufolitas Laguna del Hunco succession comprises four facies associations, with a secular trend from bottom to top indicating a shift from traction-dominated lake floor sedimentation to airfall-dominated sedimentation during lake filling.

Figure 3: Composite stratigraphic section through the Tufolitas Laguna del Hunco at Laguna del Hunco, revised from Wilf et al. (2003). Fossil localities (LH1–33), pollen sample C12 (Barreda et al., 2020) and Wilf et al. (2003) lithostratigraphic section bases (B-F; marked in the field by rebar posts) are shown in black. New U-Pb dates are shown in red, including the new U-Pb age for Ash 2211A, which previously produced an ^{40}Ar-^{39}Ar age of 52.22 ± 0.22 Ma. Note that section A of Wilf et al. (2003) is separated by a fault and not included in this profile.

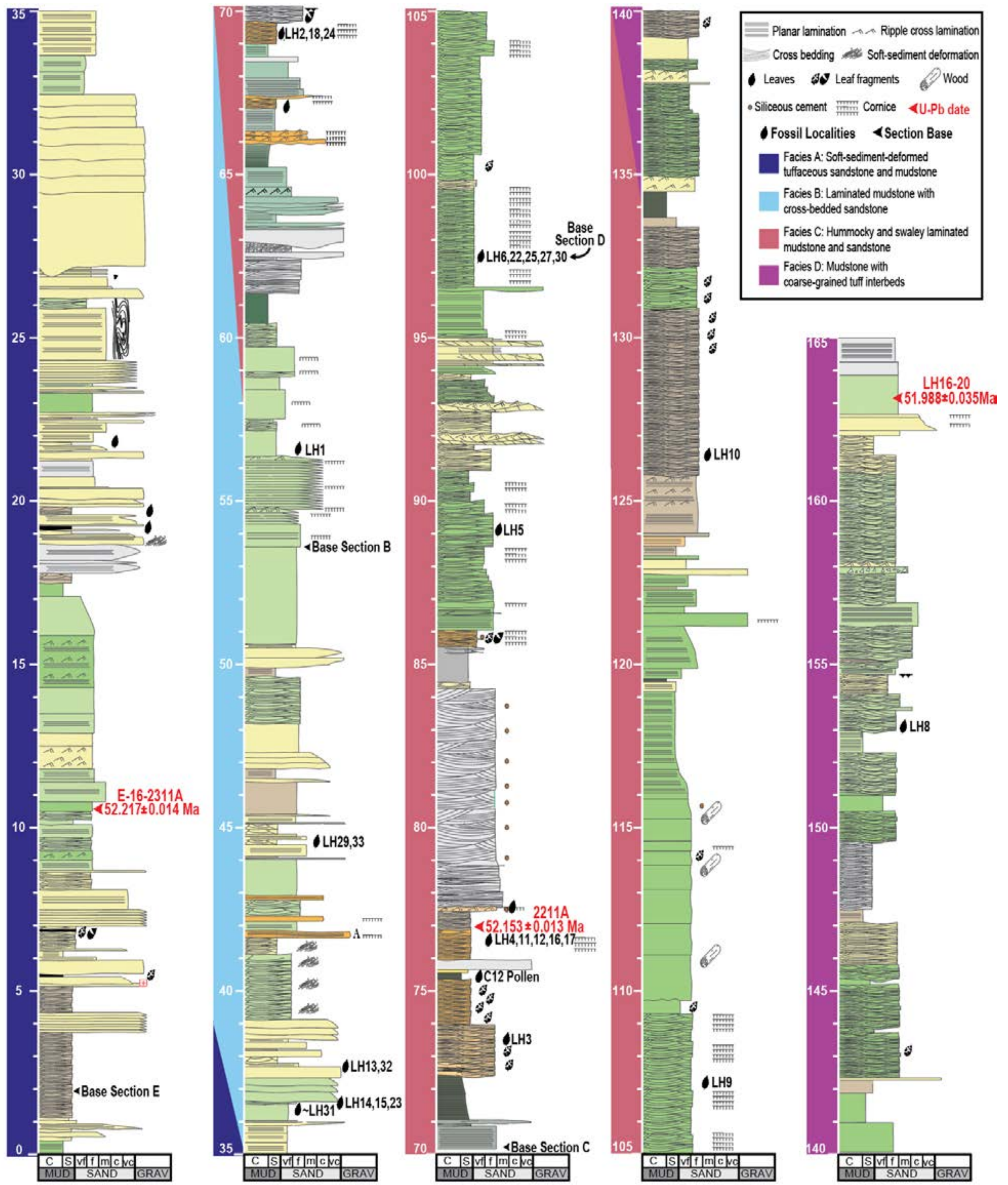
Planar lamination
Ripple cross lamination
Cross bedding
Soft-sediment deformation
Leaves
Leaf fragments
Wood
Siliceous cement
Cornice
U-Pb date
Fossil Localities
Section Base
Facies A: Soft-sediment-deformed tuffaceous sandstone and mudstone
Facies B: Laminated mudstone with cross-bedded sandstone
Facies C: Hummocky and swaley laminated mudstone and sandstone
Facies D: Mudstone with coarse-grained tuff interbeds
Base Section E
E-16-2311A
52.217±0.014 Ma
Base Section B
LH2,18,24
LH1
LH29,33
LH13,32
~LH31
LH14,15,23
Base Section D
LH6,22,25,27,30
LH5
2211A
52.153 ± 0.013 Ma
LH4,11,12,16,17
C12 Pollen
LH3
Base Section C
LH10
LH9
LH16-20
51.988±0.035Ma
LH8
C S vf f m c vc
MUD SAND GRAV

Geochronology

U-Pb dates from samples near the base and top of the exposed Laguna del Hunco deposits (Figure 3) yielded respective dates of 52.217 ± 0.014 Ma (sample E-16-2311A) and 51.998 ± 0.035 Ma (sample LH16-20; Figure 4), thus bracketing nearly all fossil deposition and macrofossil localities (LH01-LH33) to an interval of 170,000-268,000 years. Given this age control and section thickness (~153 m of section between E-16-2311A and LH16-20), long-term, average sedimentation rates for LH caldera lake infilling range from ~60-90 cm/kyr, on par with rapid long-term sedimentation rates in tectonically active basins and lakes (e.g., Xie & Heller, 2009; McNeill *et al.*, 2019; Bruck *et al.*, 2023). Additionally, reanalysis of sample 2211A (Wilf et al., 2003) refines the date in the middle of the section, near many fossil localities, to 52.153 ± 0.013 Ma (Figure 4). The three new U-Pb dates improve age precision by an order of magnitude and, for the first time, constrain the ages of nearly all fossil localities.

The new U-Pb dates place the entire LH section within chron C23r (Francescone *et al.*, 2019; Ogg, 2020), with the onset of hyperthermal event M (in C23rH2; Westerhold *et al.*, 2018; Francescone *et al.*, 2019) potentially occurring toward the top of the section. Paleomagnetic correlation with older ^{40}Ar-^{39}Ar dates from Wilf et al. (2003) ascribed the base of the LH section to chron C23n.2r and the top to chron C23n.1r. Considering the new U-Pb dates and the current geochronological framework of Eocene paleomagnetism, we interpret the previously observed reversals (Wilf et al. 2003) as short-duration, unnamed geomagnetic events within chron C23r. The potential preservation of rapid, sub-chron paleomagnetic reversals is enhanced by the high rate of LH caldera lake filling (e.g., Acton *et al.*, 2006; Zhang *et al.*, 2021).

Figure 4: U-Pb geochronology results for Laguna del Hunco tuff samples (stratigraphic positions shown in Figure 3). Left panels show concordia diagrams summarizing isotopic data, and right panels show weighted means of individual samples. Top row is sample LH16-20, middle row is the re-evaluated sample 2211A, and bottom row is sample E-16-2311A (E-16-2211A). Errors reported here are 2-sigma and include the combined analytical and tracer-calibration uncertainty and the ^{238}U decay-constant uncertainty.

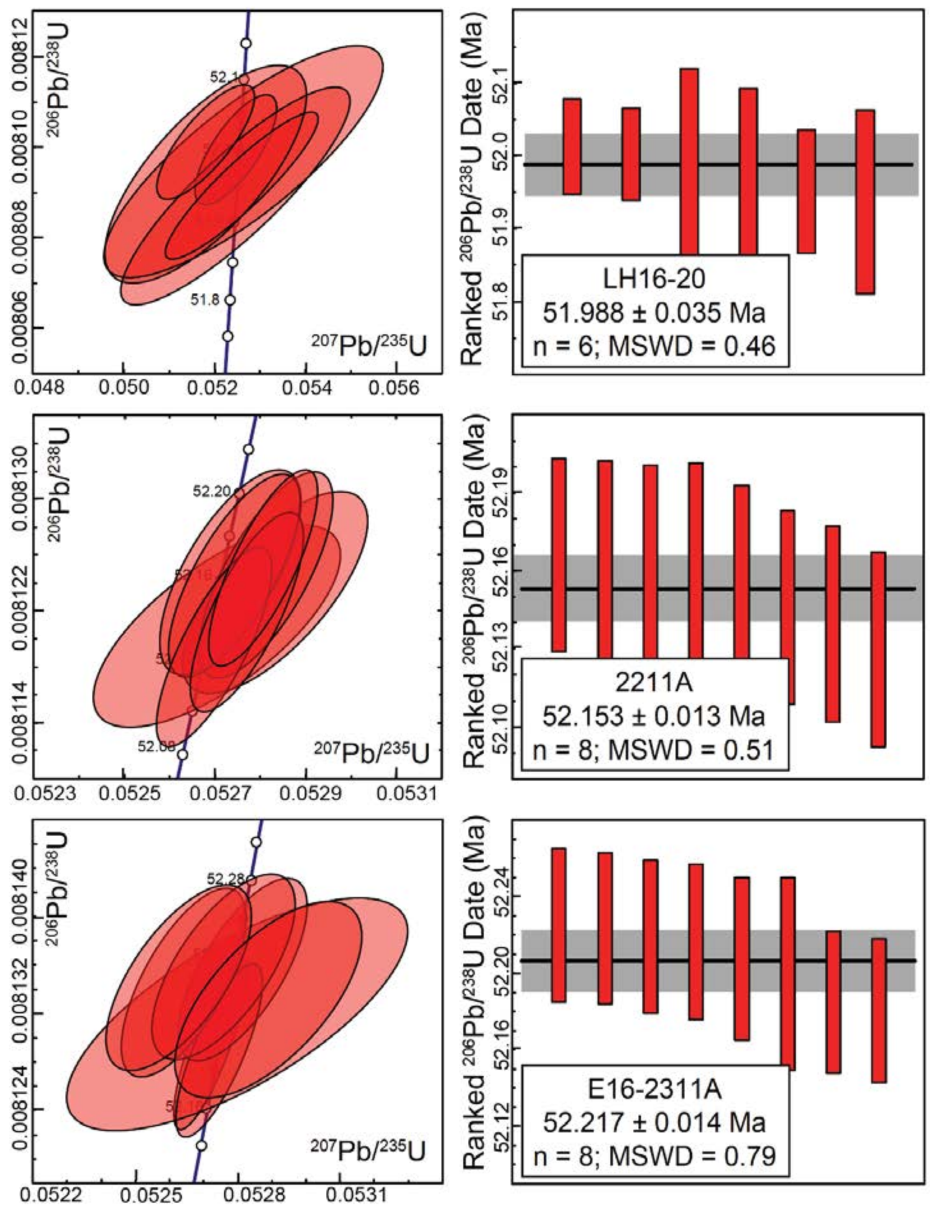

Sedimentary Facies

Overall, lithologies at the Laguna del Hunco locality are dominated by highly tuffaceous sedimentary deposits, including a range of massive, laminated, and cross-bedded mudstones and sandstones. Gosses et al., (2021) described the facies and interpreted depositional processes for LH, including laminated mudstones from hemipelagic, possibly seasonal deposition; green tuffs representing ashfall on the lake floor; and gray ashy mudstones representing basin-floor deposition. Here, we provide a detailed characterization of the facies associations (Table 1) and depositional history of LH lake filling through the geochronologically constrained section that spans key fossil localities (Figure 3).

Lithofacies descriptions

Facies Association A: Soft-sediment-deformed tuffaceous mudstone and sandstone. --- The oldest exposed sediments at Laguna del Hunco locality comprise the soft-sediment-deformed, tuffaceous mudstone and sandstone facies association. These sediments are green-gray (particularly low in the section) to tan in color (Figure 5A–G) and are predominantly composed of fine-grained tuffaceous mudstone punctuated by thin-to-thick-bedded tuffaceous sandstones. Mudstones throughout the LH deposits include clay and silt-sized particles and altered volcanic glass (Gosses et al., 2021). Occasional interbeds include mm-cm-sized clasts (Figure 5D & F). Mudstones range from structureless to laminated and sometimes exhibit graded bedding (Figure 5D). Sandstones throughout the LH succession contain volcanic clasts and minerals (e.g., biotite grains and rhyolitic clasts). Sandstones in Facies Association A generally appear structureless, but some contain planar and low-angle laminations (Figure 5C), and some bed tops show asymmetric ripple forms (Figure 5E). Soft-sediment deformation is common, including an interval of large-scale (~10m) overturned bedding packages (Figure 5B). This distinctive bed is also exposed to the south in the central caldera exposures at Puesto Alvarez – over 5 km away – where the facies is intruded by a vitric dome or laccolith (Aragón *et al.*, 2018; near Overturned beds 1-3 Study Area Map, Supplement). Additionally, smaller-scale soft-sediment deformation occurs within thicker sandstone beds throughout this facies association (e.g., Figure 5G). There are no fossil localities in this facies association, but some comminuted carbonaceous debris is present in sandstone beds and mudstones. Facies Association A appears at the base of the exposed section and transitions gradually into Facies Association B over ~5 meters.

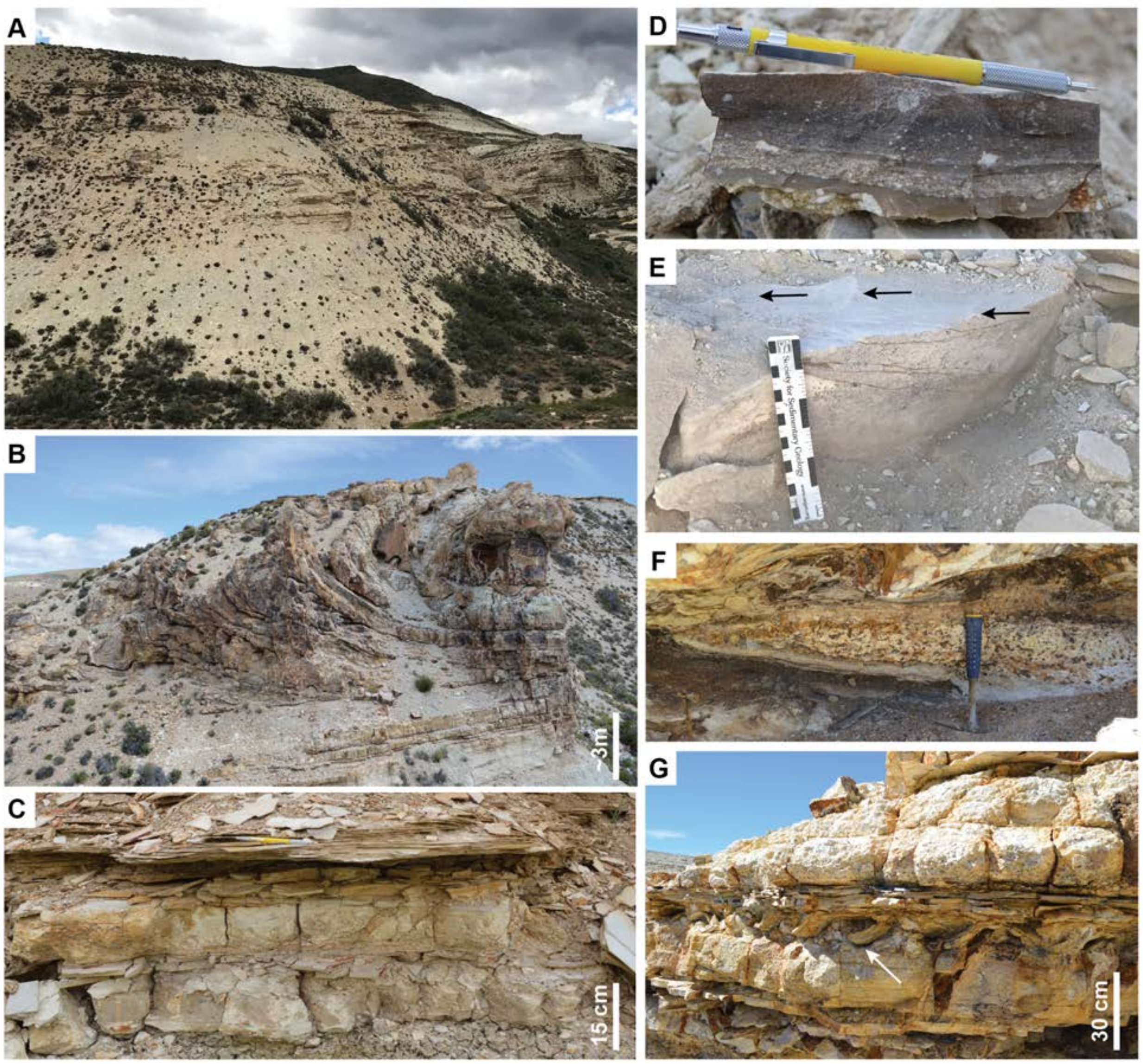

Figure 5: Example field photos of Facies A. A) Overview near Section E base and the E-16-2311A sample location; outcrop ~30 m-tall. B) Large-scale overturned bedding. C) Planar and low-angle laminated sandstone beds alternating with structureless sandstone beds. D) Small-scale fining-upward laminations. E) Asymmetric ripple bedform at the top of a sandstone bed; arrows indicate crests. F) 15 cm-thick gravelly sandstone lens. G) Alternating beds of massive sandstone, laminated sandstone, and gravelly sandstone, with one prominent soft-sediment deformed unit mimicking large-scale flame structures (arrow).

Facies Association B: Laminated tuffaceous mudstone with lenticular cross-bedded sandstone. ---Predominantly laminated mudstone and sandstone packages in this facies association are broadly lenticular-to-lobate and grade laterally into muddy deposits (Figure 6). Sand bodies are generally 4-10 m-thick and laterally extensive (>100s of meters). Internally, some sandstone bodies contain meter-scale clinoform packages that generally dip ENE. Within the sandstone bodies, massive coarse-grained tuffaceous sandstones interbed with finer laminated sandstones (Figure 6C & F). Other intervals contain dark gray-black and red-tan fine-sandstone and siltstone interbeds with Bouma (turbidite) sequences, asymmetrical ripple laminae and bedforms, planar laminations, and intervals with flame structures (Figure 6B, 6E). Sandstone packages fine upward and grade into surrounding laminated mudstone facies, at times with a downlapping geometric relationship toward the distal edges of the sandbodies. Toward the south of the study area, near locality LH-13, mudstone packages in this facies association are highly silicified and indurated with red-brown staining. This facies association includes fossil localities LH-13, LH-15, and LH-33, and it gradually transitions into Facies Association C over ~10 meters.

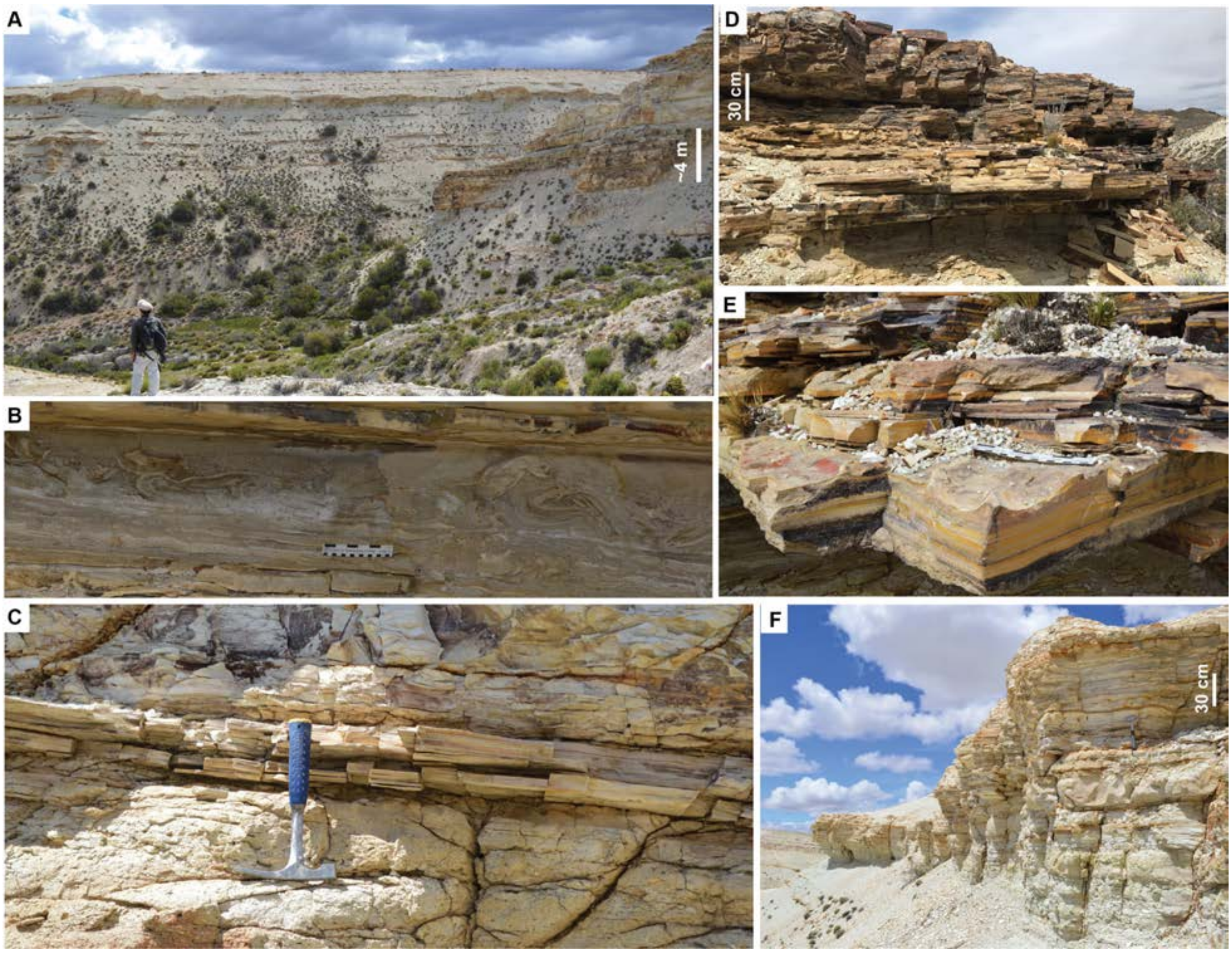

FIGURE 6: Examples of lithologies and structures in Facies Association B. A) Overview photo of outcrop near locality LH-13; distant outcrop exposure is ~40 m-thick. B) Laminated sandstones and flame structures. C) Interbedded coarse tuffaceous sandstone and laminated sandstone. D) Laminated/thin-bedded sandstone package. E) Laminated siltstone and fine sandstone. F) Example of bedding common in sandstone packages.

Facies Association C: Laminated tuffaceous mudstone and sandstone with hummocky-and-swaley beds. --- This mudstone-dominated facies association contains medium-bedded packages of fine-grained sandstone (Figure 7) and laminated mudstone intervals that contain finely interbedded layers of fine sandstone, siltstone, and claystone (Figure 7B). One interval containing locality LH-4 is particularly well-indurated and silicified, exhibiting conchoidal fractures. Red-tan staining is common on bedding planes in this facies association, and there are several laterally persistent, ~3-5 m-thick intervals of green and black mudstone, some of which have a sulfurous smell when broken (Figure 7A, C, & E). Although muddy and sandy deposits in this facies are generally tuffaceous, visible volcanic crystals are rare. Sandstone beds are finely laminated and sharp based; some are graded, and some have low-angle bedding and show hummocky-and-swaley relief (Figure 7B & D). The bed containing localities LH-6 and LH-27 is in a portion of facies C where hummocky-and-swaley bedding begins to become more common up-section. Compressed plant fossils are common throughout this facies association, which transitions to Facies Association D over an interval of ~5 m.

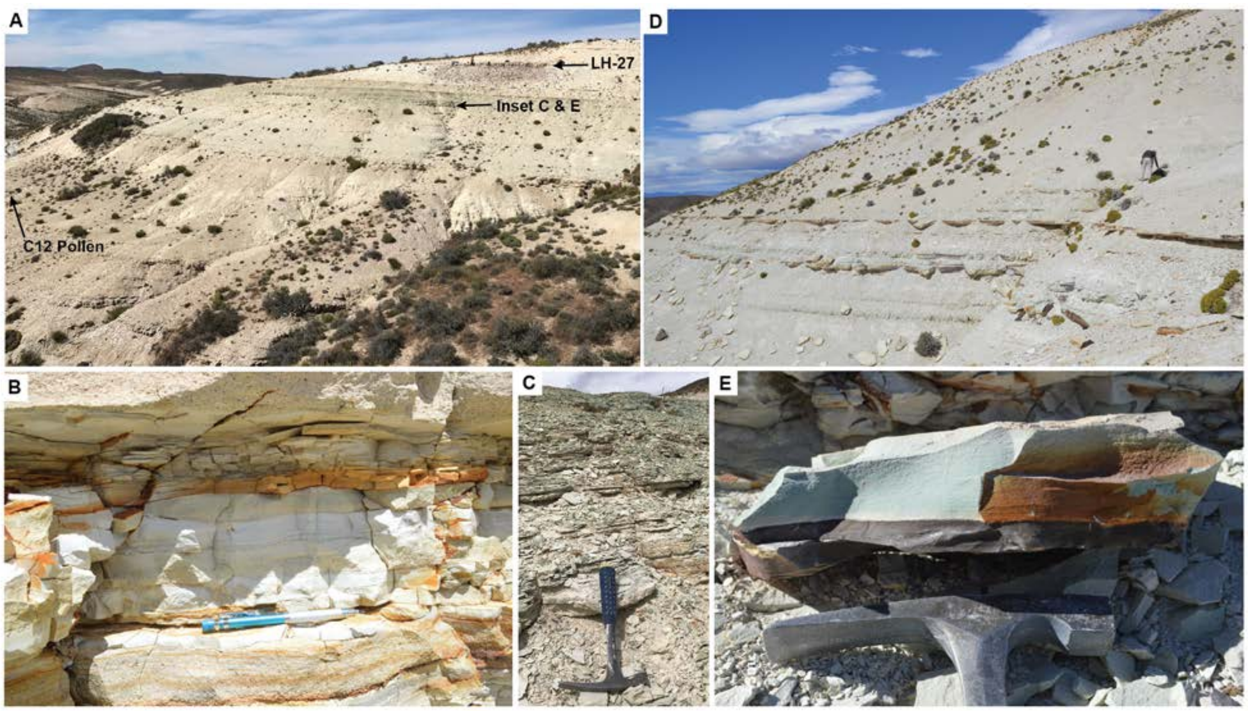

Figure 7: Field photos of Facies C features. A) Overview spanning the interval containing LH-27. Note the color zonation with red-tan (near C12 pollen), green, and white (near LH-27) intervals. B) Example of interlaminated mudstone, siltstone, and sandstone common in Facies C. C) Laminated sandstones at the base of a particularly green interval. D) Typical outcrop expression of hummocky-and-swaley bedded sandstone horizons. E) Closeup of dark gray and green laminated mudstone.

Facies Association D: Tuffaceous mudstone with coarse-grained tuff interbeds. --- Facies Association D comprises fine-grained tuffaceous mudstones punctuated with ~5-20 cm-thick, planar, tabular beds of very coarse-grained tuff layers (Figure 8). The coarse beds are tabular and laterally extensive (100s of meters). Graded bedding is common, with coarser tuffaceous layers grading into mudstone (Figure 8F & G), including features like Bouma sequences (e.g., Gosses et al., 2021). Some fossil wood material is found as float in this portion of the outcrop and originates from the overlying covered interval (Petersen, 1946; Pujana *et al.*, 2020; Brea *et al.*, 2021), and locality LH-8 sits within this facies; otherwise, there are no plant or vertebrate localities, and outcrop above the level of tuff sample LH16-20 (Figure 3) is covered with modern vegetation and fine talus.

Figure 8: Example lithologies from Facies Association D. A) Typical outcrop character of thick, coarse-grained beds. B) Sharp base of coarse tuff atop laminated siltstone. C) Example of tuff with very-coarse-sand-sized particles. D)

Laminated mudstone. E) Tuffaceous siltstone. F) Example of graded beds. G) Graded beds fining into dark gray laminated-to-structureless mudstone.

Basin-filling facies succession. --- Overall, the Laguna del Hunco basin fill trends progressively from Facies Association A to Facies Association D with gradational transitions between each facies association. The oldest exposure in the study locality is dominated by soft-sediment-deformed sandstone and mudstone (Facies Association A), exposed in the south (near the E-16-2311A U-Pb sample and the base of section E). There is a gradational shift over ~5 m to tuffaceous mudstone with lenticular cross-bedded sandstone (Facies Association B) just below localities LH-13 and LH-15. Facies Association B is well exposed laterally across the study area, and transitions to laminated tuffaceous mudstone and sandstone with hummocky-and-swaley beds (Facies Association C) over an interbedded interval ~10 m-thick between localities LH-1 and LH-2. Facies Association C becomes gradually finer grained up-section and grades into tuffaceous mudstone with coarse-grained tuff interbeds (Facies Association D) over an interval of ~10 m between localities LH-10 and LH-8.

Facies interpretations

Facies Association A – Soft-sediment-deformed tuffaceous mudstone and sandstone. --- We interpret Facies Association A as a lake-basin floor environment with fine-grained sedimentation dominated by suspension fallout (e.g., fine-grained ashfall and hemipelagic sediment) and coarser-grained deposits introduced episodically via turbidity currents and subaqueous debris flows. Soft-sediment deformation within sandstone intervals indicates pulses of rapid sedimentation and has features consistent with pyroclastic density flows (e.g., Douillet *et al.*, 2015; Zhou *et al.*, 2017). Large-scale bed turnover and extensive bed deformation (Figure 5B) are consistent with very large seismic events that imposed significant shaking across the entire caldera, disrupting an entire >10 m-thick interval of sandstone-dominated packages over >5 km of basin floor (significantly larger than other reported lacustrine seismite deposits, e.g., Doughty *et al.*, 2014; Alsop *et al.*, 2016; Shanmugam, 2016; Zhou *et al.*, 2017). We interpret water depths of this facies to have been relatively deep (10s-100s of meters) due to the predominantly fine-grained nature of the beds and lack of evidence of wave reworking. Comminuted organic debris and leaf fragments are found throughout this depositional environment, but there are no fossil localities.

Facies Association B – tuffaceous mudstone with lenticular cross-bedded sandstone. --- We interpret Facies Association B as lake-basin floor facies with well-developed subaqueous channels. Sediment in Facies B was delivered to the lake floor primarily via turbidity currents and is similar in character to other common caldera lake deposits (e.g., Nelson *et al.*, 1994; Larsen & Crossey, 1996; Otake, 2007). Channelized deepwater flows and lobes in the study area flowed broadly northeastward and redistributed coarse sediment from lake margins across the basin floor. Fine sediment in this facies most likely resulted from a combination of overbanking deepwater flows and hemipelagic sedimentation, including ash. No observations allow differentiation of water depth relative to Facies Association A, and we assume that the water depth in Facies Association B was also relatively deep. The sedimentological transition from A to B indicates a decrease in the occurrence of debris flows and high-concentration turbidity currents, along with a decrease in evidence for large-magnitude caldera shaking and a shift toward relatively organized, large-scale submarine channel distribution networks. The oldest LH fossil localities are found within the transition zone from early, tectonically active, debris-flow-dominated deposition and more organized, turbidite-channel deposition. The prevalence of highly productive fossil localities (e.g., LH13, LH15, and LH29) in this traction-dominated depositional setting indicates that intact plant material survived high-energy lake-floor flows.

Facies Association C – laminated tuffaceous mudstone and sandstone with hummocky-and-swaley beds. --- We interpret this facies association as reflecting a lake bottom environment that intermittently experiences wave energy. During the deposition of Facies Association C, material would have been delivered to the lake floor through a combination of turbidity currents and hemipelagic sedimentation, particularly lower in the interval. Evidence of wave reworking becomes increasingly common up-section, particularly near LH-27, indicating that wave influence on the lake bottom increased over time. This suggests a progressive shallowing of relative lake level from Facies Association B, although this was still a relatively deep, open lake environment with no exposed shoreline deposits. The reduction of traction-dominated transport deposits indicates a shift away from organized subaqueous channel systems on the lake floor, as seen in Facies Association B, during the deposition of Facies Association C. Most LH fossil localities, including the most productive fossil quarries, are housed within this depositional environment. The prevalence of highly silicified zones and changes from brown to white to green intervals suggest that changes in lake chemistry impacted lake floor diagenesis during this phase of deposition.

Facies Association D – tuffaceous mudstone with coarse-grained tuff interbeds. --- This facies is interpreted as reflecting airfall-derived pelagic lake sedimentation. Coarse packages blanket the region and contain large (3-5 mm) volcanic clasts and minerals, suggesting punctuated intervals of significant ashfall. This is consistent with active volcanic settings with episodic large eruptions providing a blanket of coarser ash and a background supply of fine-grained, wind-blown ash material and hemipelagic sedimentation (e.g., Cattell *et al.*, 2016; Jutzeler & McPhie, 2017). The relative lack of evidence for turbidity currents suggests that the amount of sediment delivered from point sources along the lake margin decreased in this interval, possibly due to higher overall lake levels (reducing hillslope catchment areas) and/or a relatively quiescent phase of local volcanic activity. The lack of wave influence is also consistent with higher relative lake levels in this phase of lake filling. Fossil locality LH-8 accumulated within this depositional environment, but overall, there is limited organic matter found within this phase of lake filling.

Table 1: Facies associations and environmental interpretations for the Laguna del Hunco locality.

Facies Association (Fossil Localities)	**Features**	**Occurrence and Association**	**Interpretation**
A – Soft-sediment-deformed tuffaceous mudstone and sandstone (no fossil localities)	Interbedded gray-green mudstone and thin-to-thick-bedded tuffaceous sandstone; massive beds and occasional graded bedding; occasional planar and low-angle bedding in sandstones; asymmetrical ripple forms on some bed tops; soft sediment deformation features at dm to 10-m scale	Dominates the base of the section; grades into deposits of Facies Association B over ~5 m just beneath the lowest fossil localities.	Lake floor environment receiving sediment via a combination of basal density currents (including turbidity currents and denser flows) and ash fall; deposited during a period of active caldera tectonism resulting in large-scale, regionally extensive lake-floor sediment disruption and seismite deposition.
B – Laminated tuffaceous mudstone with lenticular crossbedded sandstone (localities LH13, 14, 15, 23, 29, 31, 32, & 33)	Tan-white tuffaceous mudstone with interbedded, lenticular crossbedded sandstone bodies; sandstones contain bouma-like successions and flame structures, and interfinger with mudstones, particularly at their margins and tops	Dominant depositional style near the lower fossil localities; grades into Facies Association C over ~10 m below the middle of the fossiliferous interval	Lake floor environment dominated by subaqueous channels and fans; channelized flows conveying sediment via turbidity currents developed levees; mudstones are largely "overbank" deposits from channels lower in the section with increasing ashfall contributions higher in the section
C – Laminated tuffaceous mudstone with sandstone and hummocky-and-swaley bedding (localities LH2, 4, 5, 6, 9, 10, 11, 12, 16, 17, 18, 22, 24, 26, 27, & 30)	White-to-green finely laminated mudstone and mudstone-sandstone interbed deposits with highly silicified intervals; occasional dark gray horizons; increasing occurrence of hummocky-and-swaley cross stratified horizons toward the top of this facies association	Thickest facies association interval of the section spanning most fossil localities; trend from more event-like alternations of different colors of mudstone low in the interval to more finely laminated mudstones punctuated by hummocky-and-swaley beds higher in the interval; grades over ~5 m into Facies Association D	Lake floor deposition representing a mix of hemipelagic sedimentation, ashfall, and density flows, with density flows decreasing in abundance and ashfall increasing in abundance up-section; silicified intervals and mudstone color changes indicate more variations lake chemistry than in previous intervals; evidence of episodic

			wave reworking of the lake bed higher in this interval
D – Tuffaceous mudstone with coarse-grained tuff interbeds (locality LH8)	White and gray laminated, graded, or massive mudstone and claystone with laterally extensive, tabular, coarse-grained tuff interbeds; sharp contacts between beds with occasional deformed contacts where coarse beds overly clay beds	Capping unit of well exposed outcrop in the study area; grades into vegetated cover at the top of the section	Open lake deposits dominated by hemipelagic and airfall sedimentation; limited traction deposits compared to underlying units and significant increase in blanketing coarse-grained ashfall layers

Fossil Preservation

The quality of fossil preservation at Laguna del Hunco is exceptional, with many examples of nearly complete leaf and reproductive-organ compressions on bedding planes (Figure 2). Fossil localities are concentrated within facies associations B and C (Table 1, Figure 3), indicating two principal modes of plant fossil preservation. Vertebrate (fish, frog, turtle, and bird) and insect fossils have also been found in Facies B and C (e.g., Báez & Trueb, 1997; Azpelicueta & Cione, 2011; Petrulevičius, 2016, 2017; Degrange *et al.*, 2021) and are concentrated in the bed containing LH6 and LH27.

Well-preserved compressed plant fossils are dominantly found in laminated, fine-grained intervals of Facies B and C. In Facies B, these beds are associated with the upper, laminated mudstone deposits of Bouma sequences and hemipelagic sedimentation. Many fossil-yielding bedding planes in Facies B are found immediately above coarser intervals within a fining-upward succession, suggesting that these fossil materials were transported by and accumulated within deposits of low-density turbidity currents. Fossil localities in Facies C are found in laminated mudstone intervals interbedded with siltstones and fine sandstones that include hummocky-and-swaley cross-stratification. These occurrences indicate transport and deposition during phases of wave influence. This is consistent with plant material being introduced to the lake during wave-generating events like landslides or volcanic eruptions (e.g., Couston *et al.*, 2015; Paris, 2015; Gylfadóttir *et al.*, 2017; Paris & Ulvrova, 2019), transported to the lake bottom via turbidity currents, and subsequently resuspended and deposited during later wave reworking or combined flows impacting the lake floor. The fossiliferous facies associations (B and C) both lack coarse-grained primary ash horizons that are more common in the fossil-poor facies associations A and D. This suggests that influxes of significant coarse pyroclastic material may have been less conducive to fossil preservation than intervals dominated by sediment transported across the lake bottom.

DISCUSSION

The Tufolitas Laguna del Hunco strata at Laguna del Hunco indicate a progressive shift from high volcanic and tectonic activity to more passive infilling over the ~200,000 years of lake deposition, with an attendant shift from local, hillslope-derived sediments to more regional blankets of airborne ash material (Figure 9). Early phases of lake filling reflect a lake-floor setting that received significant, episodic influxes of pyroclastic material via density flows (e.g.. Otake, 2007; Douillet *et al.*, 2015; Cattell *et al.*, 2016) and experienced regional seismicity. Subsequently, contorted bedding and soft-sediment deformation decreased, and the dominant depositional mechanism shifted to turbidity currents transported through lake-floor channels and across lobes. Deposition via hyperpycnal flows is common where high terrestrial sediment discharges meet less-dense standing water (Mulder *et al.*, 2003); at Laguna del Hunco, this situation could have resulted from storm- or earthquake-triggered landslides (e.g., Moernaut *et al.*, 2017) from steep, caldera-rimming hillslopes and excessive biomass on overwet soils, as seen today in New Guinea (Johns, 1986). Although they are high-energy events, landslide-derived hyperpycnal flows provide an efficient pathway for transferring fresh organic material directly from hillslopes to the lake floor and immediately burying it, thereby facilitating preservation.

Delivery of fossiliferous sediment via turbidity currents continued into Facies Association C, consistent with ongoing episodic delivery of sediment from lake margins, with the addition of wave influence impacting lake-floor sediments. The predominantly fine-grained sediments in this interval suggest that lake depths were still relatively deep and that wave influence on the lake floor could have been the result of seiches or tsunami waves generated by landslides, earthquakes, or subaqueous eruptions (e.g., Belousov & Belousova, 2001; Riggs *et al.*, 2001; Couston *et al.*, 2015; Paris, 2015; Waythomas, 2022). The prevalence of low-density pyroclastic material throughout the lake fill may have allowed smaller, weaker currents and waves to mobilize sediments than would be required for quartz-dominated sediments. Turbidite-like deposits decrease through the succession into Facies Association D and are replaced by laterally persistent, tuff-rich graded beds and discrete, coarse-grained airfall deposits. The transition from turbidite-associated deposits toward discrete, laterally persistent, coarse-grained airfall deposits suggests that sediment supply shifted away from local, hillslope-derived material and toward more regionally distributed ashfall that is not reworked on the lake floor. This is consistent with higher lake levels, where increased lake area would have reduced exposed hillslope relief and catchment area feeding the lake, reducing both sediment and organic-material supply to the lake floor and cutoff density flows that could rework lake-floor deposits.

Figure 9: Schematic diagram of Laguna del Hunco depositional processes. Steep, wet, overgrown hillslopes provided a direct pathway to transfer plant material into the lake via landslides. Landslides triggered subaqueous density flows, some of which formed deepwater channels. These types of traction processes dominate deposition in much of the fossiliferous portions of the LH section. Near the middle of the section, wave activity, perhaps from

seiche or tsunami events, produced oscillatory flows that interacted with turbidity currents, creating fossil-bearing deposits with hummocky-and-swaley cross bedding. Pelagic ash deposition via airfall was present throughout lake filling but became a more prominent mechanism late in the lake-filling succession, when density flows were no longer ubiquitous.

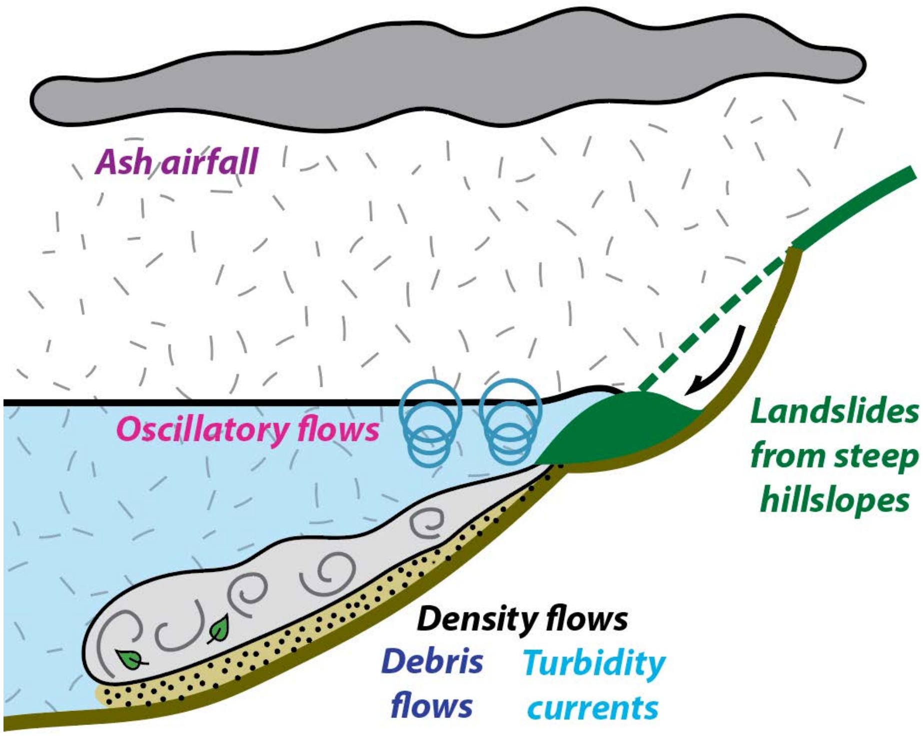

Generally, Laguna del Hunco sedimentology is consistent with well-vegetated, steep-sided, deep caldera lake depositional settings, similar to modern-day Lake Wisdom or Lake Dakataua in Papua New Guinea (e.g., Ball & Glucksman, 1978, 1980) and Lake Toba, Indonesia, which, as the world's largest caldera lake, is similar in width to the estimated diameter of the Piedra Parada caldera in which the Tufolitas Laguna del Hunco were deposited (Gosses *et al.*, 2021; Global Volcanism Program, 2024). Such landscapes experience common landslides, with dynamic, disturbance-adapted ecosystems that recover quickly to repopulate disrupted hillslopes (e.g., Johns, 1986; Saito *et al.*, 2022). Ecologically, the fossil assemblages at Laguna del Hunco are consistent with this type of setting; they show little compositional change through the section, although there are shifts in relative abundance (Wilf et al. 2005). The fossils reflect a broadly temporally stable flora with a mix of closed rainforest and adjacent woodlands. Based on nearest living relatives of the fossils, the rainforest had a rich understory and diverse angiosperm trees indicating high-relief, high rainfall environments (e.g., Merkhofer et al. 2015) as well as emergent conifers often associated with ridges and low-nutrient soils; the woodland areas had pioneer or early-successional plants that specialize in colonizing open terrain cleared by landslides and volcanic flows (e.g., *Eucalyptus*, *Macaranga*). The varying relative abundances of fossils throughout the LH section, such as the high abundances of conifers and *Eucalyptus* at the bottom and top of the main fossiliferous interval and of Anacardiaceae and Fagaceae in the middle (Wilf et al. 2005), appear to reflect stochastic landscape sampling by episodic processes like land sliding, delivering sediment and organic matter from hillslopes directly to the lake floor.

The Laguna del Hunco deposits reflect tectonically active lake conditions that differ from other modern and ancient lake settings. They are dominated by silt and clay with limited coarse material; this differs from other tectonically and volcanically active lake deposits characterized by coarse, locally derived material, like conglomerates and breccias (e.g., Gaylord *et al.*, 2001; Riggs *et al.*, 2001; Chesner, 2012). Additionally, other than a long-term shift toward higher apparent lake levels, the LH section shows no evidence of significant short-term lake-level variations outside of subtle coarsening-upward trends (pseudo-parasequences) over scales of ~10-15m (Figure 3). Lake filling and evaporation can occur rapidly (decades to centuries; e.g., Hildreth & Fierstein, 2012; Waythomas, 2022) following eruption episodes and changes in precipitation and evapotranspiration. At LH there are no occurrences of lake-margin deposits or the kinds of shoreline progradation events that are well documented in other tectonic and volcanic lake deposits, including the Eocene Green River Formation (Bruck *et al.*, 2023) and the

Oligocene Creede Formation (Larsen & Crossey, 1996). This is consistent with the lake being broad, deep, and steep sided (e.g., up to 60-degree hillslopes; Waythomas, 2022). This hypsometric profile results in very short source-to-sink sediment-transport-system lengths, where material sheds steep, wet hillslopes as landslides and mass flows and empties directly into steep-sided lakes (Figure 9). This contrasts significantly with large, tectonically active lake systems like the Eocene Green River Formation, which was fed by large catchments draining high mountains and transporting sediment and organic material many 10s of kilometers from hillslopes into the lake (e.g., Ferber & Wells, 1995). Although delivery of plant material to lakes is often attributed to windblown material settling on lake surfaces (e.g., Ferber & Wells, 1995; Gosses *et al.*, 2021), the episodic, event-like nature of the LH deposits is consistent with transfer of material – including delicate fruits and flowers – directly from hillslopes onto the lake. This rapid, episodic, event style of transport further facilitates fossil preservation by rapidly burying transported material during waning flow stages of each event.

Laguna del Hunco sedimentology and taphonomy underscore the potential for high-energy events (e.g., landslide-triggered turbidity currents) to facilitate exceptional preservation through rapid transport and burial of organic material. Landslides on a steep, wet lake margin are potentially large and energetic events (detectable seismically; e.g., Le Breton *et al.*, 2021), which quickly transfer *in situ* hillslope mass, including plants, downslope directly into the water. Once in the lake, a mass flow can be diluted with water, forming a turbidity current. Turbidity currents can further transport plant material, still largely undamaged, directly to the deep lake in a cloud of sediment-rich water and immediately bury it as the flow decelerates along the basin floor (e.g., Zavala *et al.*, 2012; Locatelli *et al.*, 2018; Kvale *et al.*, 2020). The idea that high energy flows like turbidity currents and waves damage delicate leaves and fruits can be contextualized by comparing the speeds and shear stresses associated with these flows to the forces and velocities associated with harvesting, cleaning, processing, and distributing fresh produce (e.g., Ruiz-Altisent *et al.*, 2004; Cui *et al.*, 2018). Mechanical processing and fruit and leaf damage studies show shear stresses of 1-3.5 kPa required to harvest lettuce (up to 100 mPa experienced during some washing approaches (Huang *et al.*, 2018) and 50 N or 80-120 kPa bruising apples (Yuwana & Duprat, 1997; Fu *et al.*, 2020), and velocities experienced during some harvesting and washing approaches (including for raspberries) reaching 50 cm/s (Ruiz-Altisent *et al.*, 2004; Huang *et al.*, 2018). These flow speeds are similar to documented density-flow speeds in lakes and reservoirs (Talling et al., 2013), but turbidity current experiments are associated with orders of magnitude lower basal shear stresses and pressures than produce-processing procedures (e.g., 0.001-0.05 kPa; Thompson *et al.*, 2006; Eggenhuisen & McCaffrey, 2012). High-energy mass transport provides an efficient pathway to bury fresh plant material on a lake floor, protecting it from biogeochemical degradation on land, within shallow surface waters, or on the lake bottom. Additionally, the likely low pH and high water temperatures of the volcanic lake, indicated by silica precipitation, its total lack of molluscan shell or other carbonate material, and its very low-diversity aquatic biota with only a single fish species and no aquatic insect fossils, would have further inhibited organic-material degradation.

Overall, the Laguna del Hunco deposits paint a picture of a broadly stable lake system that underwent a progressive shift from high pyroclastic input from local (hillslope) sources (Facies Association A), to turbidite and hyperpycnal sedimentation (Facies Association B) with increasing wave influence over time (Facies Association C), to airfall-dominated sedimentation with reduced local hillslope inputs and a relative lake highstand (Facies Association D). Laguna del Hunco deposition occurred near the middle of the Early Eocene Climate Optimum (Krause *et* *al.*, 2010, 2017; Hyland *et al.*, 2017; Westerhold *et al.*, 2018) during an interval of relatively stable climate (e.g., Raigemborn *et al.*, 2022). Based on comparisons with the orbitally tuned records of Westerhold et al. (2018) and the seafloor calibrated timescale of Francescone et al. (2019), the studied LH section may have spanned the C23n.2nH1 N hyperthermal event and coincided with a shift toward higher amplitude climate fluctuations. These global climate changes are not observable sedimentologically or floristically within the Laguna del Hunco section, although there is a slight increase through time in the proportion of plant species with untoothed leaves (Wilf et al. 2005).

CONCLUSIONS

The prolific Laguna del Hunco fossil localities are now better constrained geochronologically by two new U-Pb dates and a new U-Pb reanalysis of a sample that produced a previous ^{40}Ar-^{39}Ar date, bracketing deposition of the fossils between 52.217 ± 0.014 Ma to 51.988 ± 0.35 Ma. Sedimentology of the caldera lake fill indicates that rapid sedimentation facilitated exceptional preservation of plant material. Plants growing on the steep, wet hillslopes surrounding the caldera lake were most likely stochastically sampled by episodic, high-sedimentation-rate events (e.g., landslide-generated turbidity currents). This study shows how caldera lake settings can facilitate the preservation of plant Lagerstätten despite tectonism, volcanism, and highly energetic depositional processes during lake filling. This insight broadens the types of depositional settings compatible with exceptional fossil preservation.

ACKNOWLEDGEMENTS

This work was supported by NSF awards DEB-1556666 and EAR-1925755 and American Chemical Society PRF Award 60424-ND8. We thank the staff at Museo Paleontológico Egidio Feruglio (MEF) in Trelew, Argentina, especially Pablo Puerta, Mariano Caffa, and Leandro Canessa for expert logistical support in the field; Mike Donovan and M. Alejandra Gandolfo for help with field data collection; and Will Clyde for discussion of paleomagnetic data. Jason Hicks and Kirk Johnson measured the original stratigraphic section (revised here) and collected the tuff and paleomagnetic samples published in Wilf et al. (2003). We thank Secretaría de Cultura de Chubut and the Nahueltripay family for land access.

REFERENCES

Acton, G., Guyodo, Y. and Brachfeld, S. (2006) The nature of a cryptochron from a paleomagnetic study of chron C4r.2r recorded in sediments off the Antarctic Peninsula. *Physics of the Earth and Planetary Interiors*, 156, 213–222.

Aguilera, E., Mazzoni, E. and Rabassa, J. (2018) Patagonian Cenozoic magmatic activity. In: *Volcanic Landscapes and Associated Wetlands of Lowland Patagonia* (Ed. E. Mazzoni and J. Rabassa), *Springer International Publishing*, Cham, Switzerland, 31–67.

Allen, C.M. and Campbell, I.H. (2012) Identification and elimination of a matrix-induced systematic error in LA–ICP–MS $^{206}Pb/^{238}U$ dating of zircon. *Chemical Geology*, 332–333, 157–165.

Alsop, G.I., Marco, S., Weinberger, R. and Levi, T. (2016) Sedimentary and structural controls on seismogenic slumping within mass transport deposits from the Dead Sea Basin. *Sedimentary Geology*, 344, 71–90.

Anderson, R.Y., Nuhfer, E.B. and Dean, W.E. (1984) Sinking of volcanic ash in uncompacted sediment in Williams Lake, Washington. *Science*, 225, 505–508.

Andruchow-Colombo, A., Rossetto-Harris, G., Brodribb, T.J., Gandolfo, M.A. and Wilf, P. (2023) A new fossil *Acmopyle* with accessory transfusion tissue and potential reproductive buds: Direct evidence for ever-wet rainforests in Eocene Patagonia. *American Journal of Botany*, 110, e16221.

Aragón, E., Castro, A., Diaz-Alvarado, J., Pinotti, L., D′eramo, F., Demartis, M., Coniglio, J., Hernando, I. and Rodriguez, C. (2018) Mantle derived crystal-poor rhyolitic ignimbrites: Eruptive mechanism from geochemical and geochronological data of the Piedra Parada caldera, Southern Argentina. *Geoscience Frontiers*, 9, 1529–1553.

Aragón, E. and Mazzoni, M.M. (1997) Geología y estratigrafía del complejo volcánico piroclástico del Río Chubut medio (Eoceno), Chubut, Argentina. *Revista de la Asociación Geológica Argentina*, 52, 243–256.

Aragón, E. and Romero, E.J. (1984) Geología, paleoambientes y paleobotánica de yacimientos Terciarios del occidente de Río Negro, Neuquén y Chubut. *Actas del IX Congreso Geológico Argentino, San Carlos de Bariloche*, 4, 475–507.

Azpelicueta, M.D.L.M. and Cione, A.L. (2011) Redescription of the Eocene catfish *Bachmannia chubutensis* (Teleostei: Bachmanniidae) of southern South America. *Journal of Vertebrate Paleontology*, 31, 258–269.

Báez, A.M. and Trueb, L. (1997) Redescription of the Paleogene *Shelania pascuali* from Patagonia and its bearing on the relationships of fossil and recent pipoid frogs. *Scientific Papers, Natural History Museum, The University of Kansas*, 4, 1–41.

Ball, E. and Glucksman, J. (1978) Limnological studies of Lake Wisdom, a large New Guinea caldera lake with a simple fauna. *Freshwater Biology*, 8, 455–468.

Ball, E. and Glucksman, J. (1980) A limnological survey of Lake Dakataua, a large caldera lake on West New Britain, Papua New Guinea, with comparisons to Lake Wisdom, a younger nearby caldera lake. *Freshwater Biology*, 10, 73–84.

Barreda, V.D., Zamaloa, M. del C., Gandolfo, M.A., Jaramillo, C. and Wilf, P. (2020) Early Eocene spore and pollen assemblages from the Laguna del Hunco fossil lake beds, Patagonia, Argentina. *International Journal of Plant Sciences*, 181, 594–615.

Belousov, A. and Belousova, M. (2001) Eruptive process, effects and deposits of the 1996 and the ancient basaltic phreatomagmatic eruptions in Karymskoye Lake, Kamchatka, Russia. In: *Volcaniclastic Sedimentation in Lacustrine Settings* (Ed. J.D.L. White and N.R. Riggs), *John Wiley & Sons, Ltd*, Oxford, UK, 35–60.

Berry, E.W. (1925) A Miocene flora from Patagonia. *Johns Hopkins University Studies in Geology*, 6, 183–251.

Bomfleur, B. and Escapa, I. (2019) A silicified *Todea* trunk (Osmundaceae) from the Eocene of Patagonia. *PalZ*, 93, 543–548.

Brea, M., Iglesias, A., Wilf, P., Moya, E. and Gandolfo, M.A. (2021) First South American record of *Winteroxylon*, Eocene of Laguna del Hunco (Chubut, Patagonia, Argentina): new link to Australasia and Malesia. *International Journal of Plant Sciences*, 182, 185–197.

Bruck, B.T., Singer, B.S., Schmitz, M.D., Carroll, A.R., Meyers, S., Walters, A.P. and Jicha, B.R. (2023) Astronomical and tectonic influences on climate and deposition revealed through radioisotopic geochronology and Bayesian age-depth modeling of the early Eocene Green River Formation, Wyoming, USA. *GSA Bulletin*, 135, 3173–3182.

Carvalho, M.R., Wilf, P., Hermsen, E.J., Gandolfo, M.A., Cúneo, N.R. and Johnson, K.R. (2013) First record of *Todea* (Osmundaceae) in South America, from the early Eocene paleorainforests of Laguna del Hunco (Patagonia, Argentina). *American Journal of Botany*, 100, 1831–1848.

Casamiquela, R.M. (1961) Un pipoideo fósil de Patagonia. *Revista del Museo de La Plata, Sección Paleontología*, 4, 71–123.

Cattell, H., Cole, J. and Oze, C. (2016) Volcanic and sedimentary facies of the Huka Group arc-basin sequence, Wairakei–Tauhara Geothermal Field, New Zealand. *New Zealand Journal of Geology and Geophysics*, 59, 236–256.

Chesner, C.A. (2012) The Toba Caldera Complex. *Quaternary International*, 258, 5–18.

Couston, L.-A., Mei, C.C. and Alam, M.-R. (2015) Landslide tsunamis in lakes. *Journal of Fluid Mechanics*, 772, 784–804.

Cui, J., Yang, M., Son, D., Park, S. and Cho, S.-I. (2018) Estimation of tomato bruising by mechanical impact force using multivariate analysis. *HortScience*, 53, 1352–1359.

Davydov, V.I., Crowley, J.L., Schmitz, M.D. and Poletaev, V.I. (2010) High-precision U-Pb zircon age calibration of the global Carboniferous time scale and Milankovitch band cyclicity in the Donets Basin, eastern Ukraine. *Geochemistry, Geophysics, Geosystems*, 11, Q0AA04.

Deanna, R., Wilf, P. and Gandolfo, M.A. (2020) New physaloid fruit-fossil species from early Eocene South America. *American J of Botany*, 107, 1749–1762.

Degrange, F.J., Pol, D., Puerta, P. and Wilf, P. (2021) Unexpected larger distribution of paleogene stem-rollers (AVES, CORACII): new evidence from the Eocene of Patagonia, Argentina. *Scientific Reports*, 11, 1363.

Dolgopol de Sáez, M. (1941) Noticias sobre peces fósiles Argentinos. Siluroideos Terciarios de Chubut. *Notas del Museo de La Plata, Paleontología*, 6, 451–457.

Doughty, M., Eyles, N., Eyles, C.H., Wallace, K. and Boyce, J.I. (2014) Lake sediments as natural seismographs: Earthquake-related deformations (seismites) in central Canadian lakes. *Sedimentary Geology*, 313, 45–67.

Douillet, G.A., Taisne, B., Tsang-Hin-Sun, È., Müller, S.K., Kueppers, U. and Dingwell, D.B. (2015) Syn-eruptive, soft-sediment deformation of deposits from dilute pyroclastic density current: triggers from granular shear, dynamic pore pressure, ballistic impacts and shock waves. *Solid Earth*, 6, 553–572.

Eggenhuisen, J.T. and McCaffrey, W.D. (2012) Dynamic deviation of fluid pressure from hydrostatic pressure in turbidity currents. *Geology*, 40, 295–298.

Ferber, C.T. and Wells, N.A. (1995) Paleolimnology and taphonomy of some fish deposits in "Fossil" and "Uinta" Lakes of the Eocene Green River Formation, Utah and Wyoming. *Palaeogeography, Palaeoclimatology, Palaeoecology*, 117, 185–210.

Fidalgo, P. and Smith, D.R. (1987) A fossil Siricidae (Hymenoptera) from Argentina. *Entomological News*, 98, 63–66.

Francescone, F., Lauretano, V., Bouligand, C., Moretti, M., Sabatino, N., Schrader, C., Catanzariti, R., Hilgen, F., Lanci, L., Turtù, A., Sprovieri, M., Lourens, L. and Galeotti, S. (2019) A 9 million-year-long astrochronological record of the early–middle Eocene corroborated by seafloor spreading rates. *GSA Bulletin*, 131, 499–520.

Fu, H., Karkee, M., He, L., Duan, J., Li, J. and Zhang, Q. (2020) Bruise patterns of fresh market apples caused by fruit-to-fruit impact. *Agronomy*, 10, 59.

Gandolfo, M.A. and Hermsen, E.J. (2017) *Ceratopetalum* (Cunoniaceae) fruits of Australasian affinity from the early Eocene Laguna del Hunco flora, Patagonia, Argentina. *Annals of Botany*, 119, 507–516.

Gandolfo, M.A., Hermsen, E.J., Zamaloa, M.C., Nixon, K.C., González, C.C., Wilf, P., Cúneo, N.R. and Johnson, K.R. (2011) Oldest known *Eucalyptus* macrofossils are from South America. *PLoS ONE*, 6, e21084.

Gaylord, D.R., Price, S.M. and Suydam, J.D. (2001) Volcanic and hydrothermal influences on middle Eocene lacustrine sedimentary deposits, Republic Basin, northern Washington, USA. In: *Volcaniclastic Sedimentation in Lacustrine Settings* (Ed. J.D.L. White and N.R. Riggs), *Wiley*, Oxford, UK, 199–222.

Global Volcanism Program (2024) Volcanoes of the World. Distributed by Smithsonian Institution, compiled by Venzke, E. doi: https://doi.org/10.5479/si.GVP.VOTW5-2023.5.1

Gómez, J., Schobbenhaus, C. and Montes, N.E. (2019) Geological Map of South America 1:5,000,000 scale. *Colombian Geological Survey and Geological Survey of Brazil*, Commission for the Geological Map of the World (CGMW), Paris.

Gosses, J., Carroll, A.R., Bruck, B.T., Singer, B.S., Jicha, B.R., Aragón, E., Walters, A.P. and Wilf, P. (2021) Facies interpretation and geochronology of diverse Eocene floras and faunas, northwest Chubut Province, Patagonia, Argentina. *GSA Bulletin*, 133, 740–752.

Gylfadóttir, S.S., Kim, J., Helgason, J.K., Brynjólfsson, S., Höskuldsson, Á., Jóhannesson, T., Harbitz, C.B. and Løvholt, F. (2017) The 2014 Lake Askja rockslide-induced tsunami: Optimization of numerical tsunami model using observed data. *Journal of Geophysical Research: Oceans*, 122, 4110–4122.

Hildreth, W. and Fierstein, J. (2012) Eruptive history of Mount Katmai, Alaska. *Geosphere*, 8, 1527–1567.

Huang, K., Tian, Y., Salvi, D., Karwe, M. and Nitin, N. (2018) Influence of exposure time, shear stress, and surfactants on detachment of *Escherichia coli* O157:H7 from fresh lettuce leaf surfaces during washing process. *Food and Bioprocess Technology*, 11, 621–633.

Hyland, E.G., Sheldon, N.D. and Cotton, J.M. (2017) Constraining the early Eocene climatic optimum: A terrestrial interhemispheric comparison. *Geological Society of America Bulletin*, 129, 244–252.

Jaffey, A.H., Flynn, K.F., Glendenin, L.E., Bentley, W.C. and Essling, A.M. (1971) Precision measurement of half-lives and specific activities of ^{235}U and ^{238}U. *Physical Review C*, 4, 1889–1906.

Johns, R.J. (1986) The instability of the tropical ecosystem in New Guinea. *Blumea*, 31, 341–371.

Jud, N.A., Iglesias, A., Wilf, P. and Gandolfo, M.A. (2018) Fossil moonseeds from the Paleogene of West Gondwana (Patagonia, Argentina). *American Journal of Botany*, 105, 927–942.

Jutzeler, M. and McPhie, J. (2017) Field-Trip Guide to Subaqueous Volcaniclastic Facies in the Ancestral Cascades Arc in Southern Washington State—The Ohanapecosh Formation and Wildcat Creek Beds. *USGS Scientific Investigations Report 2017–5022–B*, Reston, Virginia.

Kooyman, R.M., Ivory, S.J., Benfield, A.J. and Wilf, P. (2022) Gondwanan survivor lineages and the high-risk biogeography of Anthropocene Southeast Asia. *Journal of Systematics and Evolution*, 60, 715–727.

Kooyman, R.M., Morley, R.J., Crayn, D.M., Joyce, E.M., Rossetto, M., Slik, J.W.F., Strijk, J.S., Su, T., Yap, J.-Y.S. and Wilf, P. (2019) Origins and assembly of Malesian rainforests. *Annual Review of Ecology, Evolution, and Systematics*, 50, 119–143.

Kooyman, R.M., Wilf, P., Barreda, V.D., Carpenter, R.J., Jordan, G.J., Sniderman, J.M.K., Allen, A., Brodribb, T.J., Crayn, D., Feild, T.S., Laffan, S.W., Lusk, C.H., Rossetto, M. and Weston, P.H. (2014) Paleo-Antarctic rainforest into the modern Old World tropics: The rich past and threatened future of the "southern wet forest survivors." *American Journal of Botany*, 101, 2121–2135.

Krause, J.M., Bellosi, E.S. and Raigemborn, M.S. (2010) Lateritized tephric palaeosols from Central Patagonia, Argentina: a southern high-latitude archive of Palaeogene global greenhouse conditions. *Sedimentology*, 57, 1721–1749.

Krause, J.M., Clyde, W.C., Ibañez-Mejía, M., Schmitz, M.D., Barnum, T., Bellosi, E.S. and Wilf, P. (2017) New age constraints for early Paleogene strata of central Patagonia, Argentina: Implications for the timing of South American Land Mammal Ages. *Geological Society of America Bulletin*, 129, 886–903.

Kvale, E.P., Bowie, C.M., Flenthrope, C., Mace, C., Parrish, J.M., Price, B., Anderson, S. and DiMichele, W.A. (2020) Facies variability within a mixed carbonate–siliciclastic sea-floor fan (upper Wolfcamp Formation, Permian, Delaware Basin, New Mexico). *AAPG Bulletin*, 104, 525–563.

Larsen, D. and Crossey, L.J. (1996) Depositional environments and paleolimnology of an ancient caldera lake: Oligocene Creede Formation, Colorado. *Geological Society of America Bulletin*, 108, 526.

Le Breton, M., Bontemps, N., Guillemot, A., Baillet, L. and Larose, É. (2021) Landslide monitoring using seismic ambient noise correlation: challenges and applications. *Earth-Science Reviews*, 216, 103518.

Locatelli, E.R., Briggs, D.E.G., Stemann, T.A., Portell, R.W., Means, G.H., James-Williamson, S.A. and Donovan, S.K. (2018) Leaves in marine turbidites illuminate the depositional setting of the Pliocene Bowden shell beds, Jamaica. *Geology*, 46, 131–134.

MacGinitie, H.D. (1953) Fossil plants of the Florissant beds, Colorado. *Carnegie Institution of Washington Publications*, 599, 1–198.

Matel, T.P., Gandolfo, M.A., Hermsen, E.J. and Wilf, P. (2022) Cunoniaceae infructescences from the early Eocene Laguna del Hunco flora, Patagonia, Argentina. *American Journal of Botany*, 109, 986–1003.

Mazzoni, M.M., Aragón, E. and merodio, J.C. (1989) La Ignimbrita Barda Colorada del complejo volcánico piroclástico del Río Chubut Medio. *Revista de la Asociación Geológica Argentina*, 44, 246–258.

McNeill, L.C., Shillington, D.J., Carter, G.D.O., Everest, J.D., Gawthorpe, R.L., Miller, C., Phillips, M.P., Collier, R.E.Ll., Cvetkoska, A., De Gelder, G., Diz, P., Doan, M.-L., Ford, M., Geraga, M., Gillespie, J., Hemelsdaël, R., Herrero-Bervera, E., Ismaiel, M., Janikian, L., Kouli, K., Le Ber, E., Li, S., Maffione, M., Mahoney, C., Machlus, M.L., Michas, G., Nixon, C.W., Oflaz, S.A., Omale, A.P., Panagiotopoulos, K., Pechlivanidou, S., Sauer, S., Seguin, J., Sergiou, S., Zakharova, N.V. and Green, S. (2019) High-resolution record reveals climate-driven environmental and sedimentary changes in an active rift. *Scientific Reports*, 9, 3116.

Merkhofer, L., Wilf, P., Haas, M.T., Kooyman, R.M., Sack, L., Scoffoni, C. and Cúneo, N.R. (2015) Resolving Australian analogs for an Eocene Patagonian paleorainforest using leaf size and floristics. *American Journal of Botany*, 102, 1160–1173.

Moernaut, J., Van Daele, M., Strasser, M., Clare, M.A., Heirman, K., Viel, M., Cardenas, J., Kilian, R., Ladrón de Guevara, B., Pino, M., Urrutia, R. and De Batist, M. (2017) Lacustrine turbidites produced by surficial slope sediment remobilization: A mechanism for continuous and sensitive turbidite paleoseismic records. *Marine Geology*, 384, 159–176.

Mulder, T., Syvitski, J.P.M., Migeon, S., Faugères, J.-C. and Savoye, B. (2003) Marine hyperpycnal flows: initiation, behavior and related deposits. A review. *Marine and Petroleum Geology*, 20, 861–882.

Nasdala, L., Lengauer, C.L., Hanchar, J.M., Kronz, A., Wirth, R., Blanc, P., Kennedy, A.K. and Seydoux-Guillaume, A.-M. (2002) Annealing radiation damage and the recovery of cathodoluminescence. *Chemical Geology*, 191, 121–140.

Nelson, C.H., Bacon, C.R., Robinson, S.W. and Adam, D.P. (1994) The volcanic, sedimentologic, and paleolimnologic history of the Crater Lake caldera floor, Oregon: Evidence for small caldera evolution. *Geological Society of America Bulletin*, 106, 684–704.

Ogg, J.G. (2020) Geomagnetic Polarity Time Scale. In: *Geologic Time Scale 2020* (Ed. F.M. Gradstein, J.G. Ogg, M.D. Schmitz, and G.M. Ogg), *Elsevier*, Amsterdam, Netherlands, 1, 159–192.

Otake, M. (2007) Sedimentary facies, processes and environments of the Akakura caldera lake, the South Kurikoma geothermal area, northeast Japan. *Journal of the Geological Society of Japan*, 113, 549–564.

Paris, R. (2015) Source mechanisms of volcanic tsunamis. *Philosophical Transactions of the Royal Society A*, 373, 20140380.

Paris, R. and Ulvrova, M. (2019) Tsunamis generated by subaqueous volcanic explosions in Taal Caldera Lake, Philippines. *Bulletin of Volcanology*, 81, 14.

Petersen, C.S. (1946) Estudios geológicos en la región del Río Chubut medio. *Dirección de Minas y Geología Boletín*, 59, 1–137.

Petrulevičius, J.F. (2016) A new pentatomoid bug from the Ypresian of Patagonia, Argentina. *Acta Palaeontologica Polonica*, 61, 863–868.

Petrulevičius, J.F. (2017) A new burmagomphid dragonfly from the Eocene of Patagonia, Argentina. *Acta Palaeontologica Polonica*, 62, 779–783.

Pujana, R.R., Wilf, P. and Gandolfo, M.A. (2020) Conifer wood assemblage dominated by Podocarpaceae, early Eocene of Laguna del Hunco, central Argentinean Patagonia. *PhytoKeys*, 156, 81–102.

Raigemborn, M.S., Lizzoli, S., Hyland, E., Cotton, J., Gómez Peral, L.E., Beilinson, E. and Krause, J.M. (2022) A paleopedological approach to understanding Eocene environmental conditions in southern Patagonia, Argentina. *Palaeogeography, Palaeoclimatology, Palaeoecology*, 601, 111129.

Riggs, N.R., Ort, M.H., White, J.D.L., Wilson, C.J.N., Houghton, B.F. and Clarkson, R. (2001) Post-1.8-ka marginal sedimentation in Lake Taupo, New Zealand: Effects of wave energy and sediment supply in a rapidly rising lake. In: *Volcaniclastic Sedimentation in Lacustrine Settings* (Ed. J.D.L. White and N.R. Riggs), *Wiley*, Oxford, UK, 151–177.

Romero, E.J. (1986) Paleogene phytogeography and climatology of South America. *Annals of the Missouri Botanical Garden*, 73, 449–461.

Romero, E.J. and Hickey, L.J. (1976) A fossil leaf of Akaniaceae from Paleocene beds in Argentina. *Bulletin of the Torrey Botanical Club*, 103, 126–131.

Rossetto-Harris, G., Wilf, P., Escapa, I.H. and Andruchow-Colombo, A. (2020) Eocene *Araucaria* Sect. *Eutacta* from Patagonia and floristic turnover during the initial isolation of South America. *American Journal of Botany*, 107, 806–832.

Ruiz-Altisent, M., Ortiz-Cañavate, J. and Valero, C. (2004) Fruit and vegetables harvesting systems. In: *Production Practices and Quality Assessment of Food Crops Volume 1: Preharvest Practice* (Ed. R. Dris and S.M. Jain), *Springer Netherlands*, Dordrecht, 261–285.

Saito, H., Uchiyama, S. and Teshirogi, K. (2022) Rapid vegetation recovery at landslide scars detected by multitemporal high-resolution satellite imagery at Aso volcano, Japan. *Geomorphology*, 398, 107989.

Schmitz, M.D. and Davydov, V.I. (2012) Quantitative radiometric and biostratigraphic calibration of the Pennsylvanian-Early Permian (Cisuralian) time scale and pan-Euramerican chronostratigraphic correlation. *Geological Society of America Bulletin*, 124, 549–577.

Schmitz, M.D. and Schoene, B. (2007) Derivation of isotope ratios, errors, and error correlations for U-Pb geochronology using ^{205}Pb- ^{235}U-(^{233}U)-spiked isotope dilution thermal ionization mass spectrometric data. *Geochemistry, Geophysics, Geosystems*, 8, Q08006.

Shanmugam, G. (2016) The seismite problem. *Journal of Palaeogeography*, 5, 318–362.

Smith, D.M. (2012) Exceptional preservation of insects in lacustrine environments. *PALAIOS*, 27, 346–353.

Somoza, R. (2007) Eocene paleomagnetic pole for South America: Northward continental motion in the Cenozoic, opening of Drake Passage and Caribbean convergence. *Journal of Geophysical Research*, 112, B03104.

Thompson, C.E.L., Amos, C.L., Angelaki, M., Jones, T.E.R. and Binks, C.E. (2006) An evaluation of bed shear stress under turbid flows. *Journal of Geophysical Research: Oceans*, 111, C04008.

Varekamp, J.C. (2015) The chemical composition and evolution of volcanic lakes. In: *Volcanic Lakes* (Ed. D. Rouwet, B. Christenson, F. Tassi, and J. Vandemeulebrouck), *Springer*, Berlin, Heidelberg, 93–123.

Waythomas, C.F. (2022) Selected crater and small caldera lakes in Alaska: Characteristics and hazards. *Frontiers in Earth Science*, 9, 751216.

Westerhold, T., Röhl, U., Donner, B. and Zachos, J.C. (2018) Global extent of Early Eocene hyperthermal events: A new Pacific benthic foraminiferal isotope record from Shatsky Rise (ODP Site 1209). *Paleoceanography and Paleoclimatology*, 33, 626–642.

Wilf, P. (2012) Rainforest conifers of Eocene Patagonia: Attached cones and foliage of the extant Southeast Asian and Australasian genus *Dacrycarpus* (Podocarpaceae). *American Journal of Botany*, 99, 562–584.

Wilf, P., Carvalho, M.R., Gandolfo, M.A. and Cúneo, N.R. (2017) Eocene lantern fruits from Gondwanan Patagonia and the early origins of Solanaceae. *Science*, 355, 71–75.

Wilf, P., Cúneo, N.R., Escapa, I.H., Pol, D. and Woodburne, M.O. (2013) Splendid and seldom isolated: The paleobiogeography of Patagonia. *Annual Review of Earth and Planetary Sciences*, 41, 561–603.

Wilf, P., Cúneo, N.R., Johnson, K.R., Hicks, J.F., Wing, S.L. and Obradovich, J.D. (2003) High plant diversity in Eocene South America: Evidence from Patagonia. *Science*, 300, 122–124.

Wilf, P., Escapa, I.H., Cúneo, N.R., Kooyman, R.M., Johnson, K.R. and Iglesias, A. (2014) First South American *Agathis* (Araucariaceae), Eocene of Patagonia. *American Journal of Botany*, 101, 156–179.

Wilf, P., González, C.C., Gandolfo, M.A. and Zamaloa, M.C. (2024) Putative *Celtis* leaves from Eocene Patagonia are allied with Asian Anacardiaceae. *Ameghiniana*, 61, 73–93.

Wilf, P., Iglesias, A. and Gandolfo, M.A. (2023) The first Gondwanan Euphorbiaceae fossils reset the biogeographic history of the *Macaranga-Mallotus* clade. *American Journal of Botany*, 110, e16169.

Wilf, P., Johnson, K.R., Cúneo, N.R., Smith, M.E., Singer, B.S. and Gandolfo, M.A. (2005) Eocene plant diversity at Laguna del Hunco and Río Pichileufú, Patagonia, Argentina. *The American Naturalist*, 165, 634–650.

Wilf, P., Nixon, K.C., Gandolfo, M.A. and Cúneo, N.R. (2019) Eocene Fagaceae from Patagonia and Gondwanan legacy in Asian rainforests. *Science*, 364, eaaw5139.

Xie, X. and Heller, P. (2009) Plate tectonics and basin subsidence history. *Geological Society of America Bulletin*, 121, 55–64.

Yuwana, Y. and Duprat, F. (1997) Prediction of apple bruising based on the instantaneous impact shear stress and energy absorbed. *International Agrophysics*, 11, 215–222.

Zamaloa, M. del C., Gandolfo, M.A., González, C.C., Romero, E.J., Cúneo, N.R. and Wilf, P. (2006) Casuarinaceae from the Eocene of Patagonia, Argentina. *International Journal of Plant Sciences*, 167, 1279–1289.

Zamaloa, M.C., Gandolfo, M.A. and Nixon, K.C. (2020) 52 million years old *Eucalyptus* flower sheds more than pollen grains. *American Journal of Botany*, 107, 1763–1771.

Zavala, C., Arcuri, M. and Blanco Valiente, L. (2012) The importance of plant remains as diagnostic criteria for the recognition of ancient hyperpycnites. *Revue de Paléobiologie, Genève*, 11, 457–469.

Zhang, R., Kravchinsky, V.A., Qin, J., Goguitchaichvili, A. and Li, J. (2021) One and a half million yearlong aridity during the middle Eocene in north-west China linked to a global cooling episode. *Journal of Geophysical Research: Solid Earth*, 126, e2020JB021037.

Zhou, Y.-Q., Peng, T.-M., Zhou, T.-F., Zhang, Z.-K., Tian, H., Liang, W.-D., Yu, T. and Sun, L.-F. (2017) Soft-sediment deformation structures related to volcanic earthquakes of the Lower Cretaceous Qingshan Group in Lingshan Island, Shandong Province, East China. *Journal of Palaeogeography*, 6, 162–181.

SUPPLEMENTARY INFORMATION

Study area and locality information

The Laguna del Hunco study area lies in a protected area of Chubut Province, and sampling without a permit is illegal. Access to the land requires careful coordination with provincial authorities and local landowners. Qualified researchers should contact the Museo Paleontológico Egidio Feruglio – MEF – for more information about accessing the localities: https://mef.org.ar/home/

A digital map of the localities included in this paper is available here, where a csv or kml/kmz file of locality coordinates can be downloaded (click on the three dots "Layer Options" menu and select "Export Data": https://www.google.com/maps/d/edit?mid=1QcF_CK9HAvgoT3uIgoTjN4qPTL1jzMQ&usp=sharing

Map layers include paleontology localities, geochronological localities from this study, sedimentological features of interest, and all GPS-located points from the paleomag section of Wilf et al., (2003). Localities LH26 and some sedimentological features are outside of the extent of the study area map shown in Figure 1 of the main manuscript.

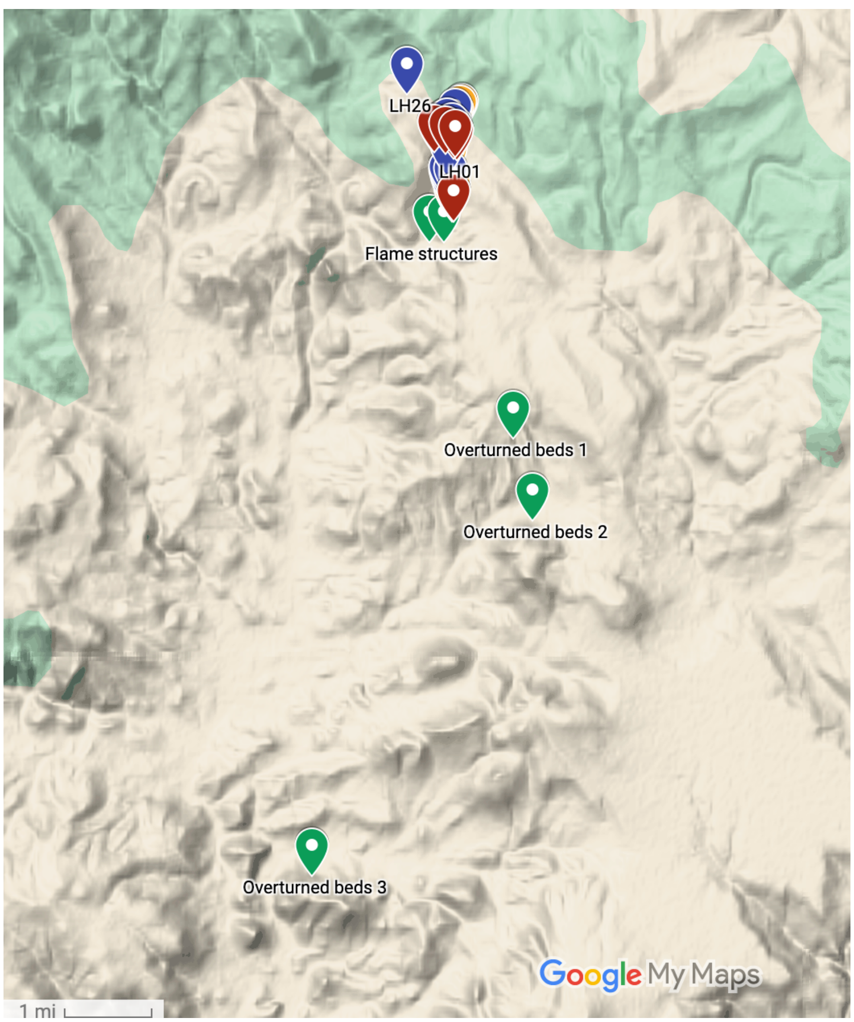

Name	Type	Lat	Lon	Notes
E-16-2311A	section_geochron	-42.470875	-70.036224	Re-sampled 2311A (from Wilf et al. 2003) during 2016 field season
LH16-20	section_geochron	-42.460055	-70.040256	Upper Tuff from 2016 field season
Base of Section B	section_geochron	-42.461267	-70.035477	2016 Field Season
Base of Section C	section_geochron	-42.461064	-70.036129	2016 Field Season
Base of Section D	section_geochron	-42.46025	-70.037944	2016 Field Season
Base of Section E	section_geochron	-42.470903	-70.036027	2016 Field Season
2211A	section_geochron	-42.460699	-70.035857	Bed C25 of Hicks (Wilf et al. 2003); No GPS from original collection; location estimated in 2016 as 0.6 m above LH4 locality
LH01	fossil_locality	-42.461257	-70.035267	2016 Field Season
LH02	fossil_locality	-42.460892	-70.035736	2016 Field Season
LH03-04	fossil_locality	-42.460699	-70.035857	2016 Field Season
LH05	fossil_locality	-42.460291	-70.036807	2016 Field Season
LH06-07	fossil_locality	-42.459884	-70.036302	2016 Field Season
LH08	fossil_locality	-42.459776	-70.039322	2016 Field Season
LH09	fossil_locality	-42.459755	-70.0373	2016 Field Season
LH10	fossil_locality	-42.45924	-70.038335	2016 Field Season
LH13	fossil_locality	-42.467523	-70.036715	2016 Field Season
LH15	fossil_locality	-42.467887	-70.036796	2016 Field Season
LH16	fossil_locality	-42.461794	-70.036082	2016 Field Season
LH18	fossil_locality	-42.462416	-70.036839	2016 Field Season
LH20	fossil_locality	-42.457888	-70.035852	2016 Field Season
LH21	fossil_locality	-42.457352	-70.03576	2016 Field Season
LH22	fossil_locality	-42.460892	-70.037654	2016 Field Season
LH23	fossil_locality	-42.468639	-70.037638	2016 Field Season
LH24	fossil_locality	-42.460077	-70.035884	2016 Field Season
LH25	fossil_locality	-42.458883	-70.03753	2016 Field Season
LH27	fossil_locality	-42.4613	-70.037037	2016 Field Season
LH28	fossil_locality	-42.460149	-70.03771	2016 Field Season
LH29	fossil_locality	-42.46691	-70.03773	3/13/2019; about 7 m above LH13
LH30	fossil_locality	-42.45969	-70.03633	3/16/2019; extension of LH6
LH31	fossil_locality	-42.46747	-70.03781	below LH15 level in the gully
LH32	fossil_locality	-42.46711	-70.0379	3/17/2023; same level as LH13
LH33	fossil_locality	-42.46739	-70.03679	3/21/2023; same level as LH29
LH26	fossil_locality	-42.450722	-70.046097	Wilf et al (2003)
C12Pollen	fossil_locality	-42.460522	-70.037139	2016 Field Season; Organic-rich bed C12 (Wilf et al. 2003)
LH17	fossil_locality	-42.46366667	-70.03738889	Wilf et al (2003)
Overturned beds 1	sedimentary_feature	-42.505	-70.02333	Southern Overturned Beds (Ojo de Cleopatra)
Overturned beds 2	sedimentary_feature	-42.51788	-70.01946	southward of Cleopatra's eye
Overturned beds 3	sedimentary_feature	-42.57375	-70.06649	southward, 2021
Flame structures (Figure 6B)	sedimentary_feature	-42.47411	-70.04128	Figure 6B
Overturned beds (Figure 5B)	sedimentary_feature	-42.47406	-70.03817	Figure 5B

Geochronology

Errors reported here include the combined analytical and tracer-calibration uncertainty, and uncertainty in the ^{238}U decay-constant uncertainty.

An abundant population of relatively large, (approximately 100-300 micron in long dimension), elongate, prismatic zircon crystals was separated from a hand sample of each sample by conventional density and magnetic methods. The entire zircon separate was placed in a muffle furnace at 900°C for 60 hours in quartz beakers to anneal minor radiation damage; annealing enhances cathodoluminescence (CL) emission (Nasdala et al., 2002), promotes more reproducible interelement fractionation during laser ablation inductively coupled plasma mass spectrometry (LA-ICPMS) (Allen and Campbell, 2012), and prepares the crystals for subsequent chemical abrasion (Mattinson, 2005). Following annealing, individual grains from three samples (E16-2311A, LH16-20, 03/17-489) were hand-picked. No mounting or imaging was required as the majority of the zircon were elongate and prismatic, indicative of primary igneous zircon.

U-Pb geochronology methods for isotope dilution thermal ionization mass spectrometry follow those previously published by Davydov et al. (2010) and Schmitz and Davydov (2012). Zircon crystals were subjected to a modified version of the chemical abrasion method of Mattinson (2005), whereby single crystal fragments plucked from grain mounts were individually abraded in a single step with concentrated HF at 180°C for 12 hours. U-Pb dates and uncertainties for each analysis were calculated using the algorithms of Schmitz and Schoene (2007) and the U decay constants of Jaffey et al. (1971). Uncertainties are based upon non-systematic analytical errors, including counting statistics, instrumental fractionation, tracer subtraction, and blank subtraction. These error estimates should be considered when comparing our $^{206}Pb/^{238}U$ dates with those from other laboratories that used tracer solutions calibrated against the EARTHTIME gravimetric standards. When comparing our dates with those derived from other decay schemes (e.g., $^{40}Ar/^{39}Ar$, ^{187}Re-^{187}Os), the uncertainties in tracer calibration (0.03%; Condon et al., 2015; McLean et al., 2015) and U decay constants (0.108%; Jaffey et al., 1971) should be added to the internal error in quadrature. Quoted errors for calculated weighted means are thus of the form ±X(Y)[Z], where X is solely analytical uncertainty, Y is the combined analytical and tracer uncertainty, and Z is the combined analytical, tracer and ^{238}U decay constant uncertainty.

E16-2311A: Eight zircon crystals were selected for CA-TIMS based morphology and the absence of inclusions. Chemical abrasion in concentrated HF at 190° for 12 hours resulted in only moderate dissolution of the zircon crystals. All eight analyses are concordant and equivalent, with a weighted mean $^{206}Pb/^{238}U$ date of 52.217 ± 0.014(0.03)[0.06] Ma (MSWD = 0.79), which is interpreted as dating the eruption and deposition of this tuff sample.

LH16-20: Six zircon crystals were selected for CA-TIMS based morphology and the absence of inclusions. Chemical abrasion in concentrated HF at 190° for 12 hours resulted in only moderate dissolution of the zircon crystals. All six analyses are concordant and equivalent, with a weighted mean $^{206}Pb/^{238}U$ date of 51.988 ± 0.035(0.04)[0.07] Ma (MSWD = 0.46), which is interpreted as dating the eruption and deposition of this tuff sample.

CA-TIMS U-Pb isotopic data

Sample (a)	Compositional Parameters: Th/U (b)	$^{206}Pb^*$ $\times 10^{-13}$ mol (c)	mol % $^{206}Pb^*$ (c)	Pb^*/Pb_c (c)	Pb_c (pg) (c)	$^{206}Pb/^{204}Pb$ (d)	Radiogenic Isotope Ratios: $^{208}Pb/^{206}Pb$ (e)	$^{207}Pb/^{206}Pb$ (e)	% err (f)	$^{207}Pb/^{235}U$ (e)	% err (f)	$^{206}Pb/^{238}U$ (e)	% err (f)	corr. coef.	Isotopic Ages: $^{207}Pb/^{206}Pb$ (g)	± (f)	$^{207}Pb/^{235}U$ (g)	± (f)	$^{206}Pb/^{238}U$ (g)	± (f)
E16-2311A																				
z1	0.680	0.7921	99.69%	102	0.20	5866	0.218	0.04703	0.118	0.052719	0.167	0.008130	0.072	0.813	50.9	2.8	52.17	0.08	**52.19**	**0.04**
z2	0.543	0.3593	97.04%	10	0.91	609	0.174	0.04709	0.709	0.052797	0.774	0.008132	0.097	0.714	53.7	16.9	52.24	0.39	**52.21**	**0.05**
z3	0.642	0.1960	99.06%	33	0.15	1918	0.206	0.04708	0.248	0.052813	0.293	0.008136	0.076	0.698	53.4	5.9	52.26	0.15	**52.23**	**0.04**
z4	0.594	0.5428	99.47%	58	0.24	3417	0.191	0.04706	0.148	0.052744	0.195	0.008129	0.072	0.779	52.2	3.5	52.19	0.10	**52.19**	**0.04**
z5	0.662	0.2074	99.15%	37	0.15	2127	0.212	0.04693	0.239	0.052640	0.285	0.008135	0.078	0.684	45.8	5.7	52.09	0.14	**52.23**	**0.04**
z6	0.674	0.2719	98.98%	30	0.23	1767	0.216	0.04703	0.281	0.052757	0.325	0.008136	0.077	0.668	50.7	6.7	52.20	0.17	**52.24**	**0.04**
z7	0.674	0.3380	98.96%	30	0.29	1738	0.216	0.04692	0.287	0.052624	0.330	0.008135	0.077	0.664	45.0	6.8	52.08	0.17	**52.23**	**0.04**
z8	0.626	0.2709	98.56%	21	0.33	1255	0.201	0.04716	0.378	0.052888	0.424	0.008133	0.082	0.645	57.5	9.0	52.33	0.22	**52.22**	**0.04**
LH16-20																				
z1	1.050	0.1078	0.9532	7	0.44	386	0.337	0.04697	1.313	0.052453	1.400	0.008100	0.122	0.745	47.6	31.3	51.91	0.71	**52.00**	**0.06**
z2	0.502	0.0485	0.9117	3	0.39	204	0.161	0.04713	2.476	0.052577	2.624	0.008091	0.164	0.911	55.7	59.0	52.03	1.33	**51.95**	**0.08**
z3	0.506	0.0430	0.9114	3	0.35	204	0.163	0.04701	3.731	0.052433	3.940	0.008089	0.244	0.871	49.8	89.0	51.89	1.99	**51.94**	**0.13**
z4	0.510	0.0354	0.8571	2	0.49	126	0.164	0.04713	4.573	0.052615	4.782	0.008097	0.259	0.816	55.8	##	52.07	2.43	**51.99**	**0.13**
z5	0.456	0.0578	0.8296	1	0.99	106	0.146	0.04640	3.320	0.051781	3.492	0.008094	0.243	0.724	18.4	79.7	51.26	1.75	**51.97**	**0.13**
z6	0.694	0.0626	0.9481	6	0.28	348	0.223	0.04636	1.596	0.051786	1.694	0.008101	0.127	0.789	16.5	38.3	51.27	0.85	**52.01**	**0.07**
2211A																				
z1	0.674	0.8187	99.37%	50	0.43	2866	0.216	0.04708	0.181	0.052742	0.226	0.008125	0.073	0.735	53.4	4.3	52.19	0.12	**52.16**	**0.04**
z2	0.902	0.4875	99.54%	72	0.19	3915	0.29	0.04707	0.2	0.052733	0.242	0.008125	0.074	0.683	52.9	4.8	52.18	0.12	**52.16**	**0.04**
z3	0.658	0.7199	99.41%	53	0.35	3060	0.211	0.04714	0.183	0.052811	0.229	0.008125	0.075	0.725	56.5	4.4	52.26	0.12	**52.16**	**0.04**
z4	0.488	0.2236	99.07%	32	0.17	1947	0.157	0.04707	0.377	0.052702	0.423	0.008121	0.073	0.704	52.7	9	52.15	0.21	**52.14**	**0.04**
z5	0.644	0.515	99.07%	33	0.4	1942	0.207	0.04717	0.271	0.052831	0.316	0.008123	0.073	0.705	57.8	6.5	52.27	0.16	**52.16**	**0.04**
z6	0.604	0.4165	99.59%	75	0.14	4390	0.194	0.04707	0.15	0.052697	0.198	0.008119	0.072	0.783	52.9	3.6	52.15	0.1	**52.13**	**0.04**
z7	0.582	0.719	99.68%	95	0.19	5584	0.187	0.04714	0.139	0.052806	0.185	0.008125	0.071	0.778	56.1	3.3	52.25	0.09	**52.17**	**0.04**
z8	0.85	0.5579	99.62%	87	0.18	4788	0.273	0.04712	0.147	0.052769	0.192	0.008122	0.072	0.756	55.4	3.5	52.21	0.1	**52.15**	**0.04**

Weighted Mean Calculations (h)

E16-2311A

$^{206}Pb/^{238}U$ ± random (+tracer) [+λ]		MSWD	prob. Fit
52.217 ± 0.014 (0.03) [0.06]	**± 2s int.**	**0.79**	0.591
± 0.015 (0.03) [0.06]	**± 95% c.i.***	**n =**	8

LH16-20

$^{206}Pb/^{238}U$ ± random (+tracer) [+λ]		MSWD	prob. Fit
51.988 ± 0.035 (0.04) [0.07]	**± 2s int.**	**0.46**	0.804
± 0.031 (0.04) [0.07]	**± 95% c.i.***	**n =**	6

2211A

$^{206}Pb/^{238}U$ ± random (+tracer) [+λ]		MSWD	prob. Fit
52.15 ± 0.013 (0.03) [0.06]	**± 2s int.**	**0.51**	0.827
± 0.011 (0.03) [0.06]	**± 95% c.i.***	**n =**	8

(a) z1, z2 etc. are labels for single zircon grains or fragments annealed and chemically abraded after Mattinson (2005); **bold** indicates results used in weighted mean calculations.
(b) Model Th/U ratio iteratively calculated from the radiogenic 208Pb/206Pb ratio and 206Pb/238U age.
(c) Pb* and Pbc represent radiogenic and common Pb, respectively; mol % $^{206}Pb^*$ with respect to radiogenic, blank and initial common Pb.
(d) Measured ratio corrected for spike and fractionation only. Fractionation estimated at 0.17 +/- 0.03 %/a.m.u. for Daly analyses, based on analysis of NBS-981 and NBS-982.
(e) Corrected for fractionation, spike, and common Pb; all common Pb was assumed to be procedural blank: 206Pb/204Pb = 18.042 ± 0.61%; 207Pb/204Pb = 15.537 ± 0.52%; 208Pb/204Pb = 37.686 ± 0.63% (all uncertainties 1-sigma).
(f) Errors are 2-sigma, propagated using the algorithms of Schmitz and Schoene (2007).
(g) Calculations are based on the decay constants of Jaffey et al. (1971). 206Pb/238U and 207Pb/206Pb ages corrected for initial disequilibrium in 230Th/238U using Th/U [magma] = 3.
(h) λ = decay constant; MSWD = mean squared weighted deviation; prob. fit = chi-squared distribution probability; 95% confidence interval = σ * Student's T multiplier * (MSWD)^0.5.

Simplified composite graphical log

Simplified graphical log showing the stratigraphic position of fossil localities (black), U-Pb dates (red), and important depositional processes through time.

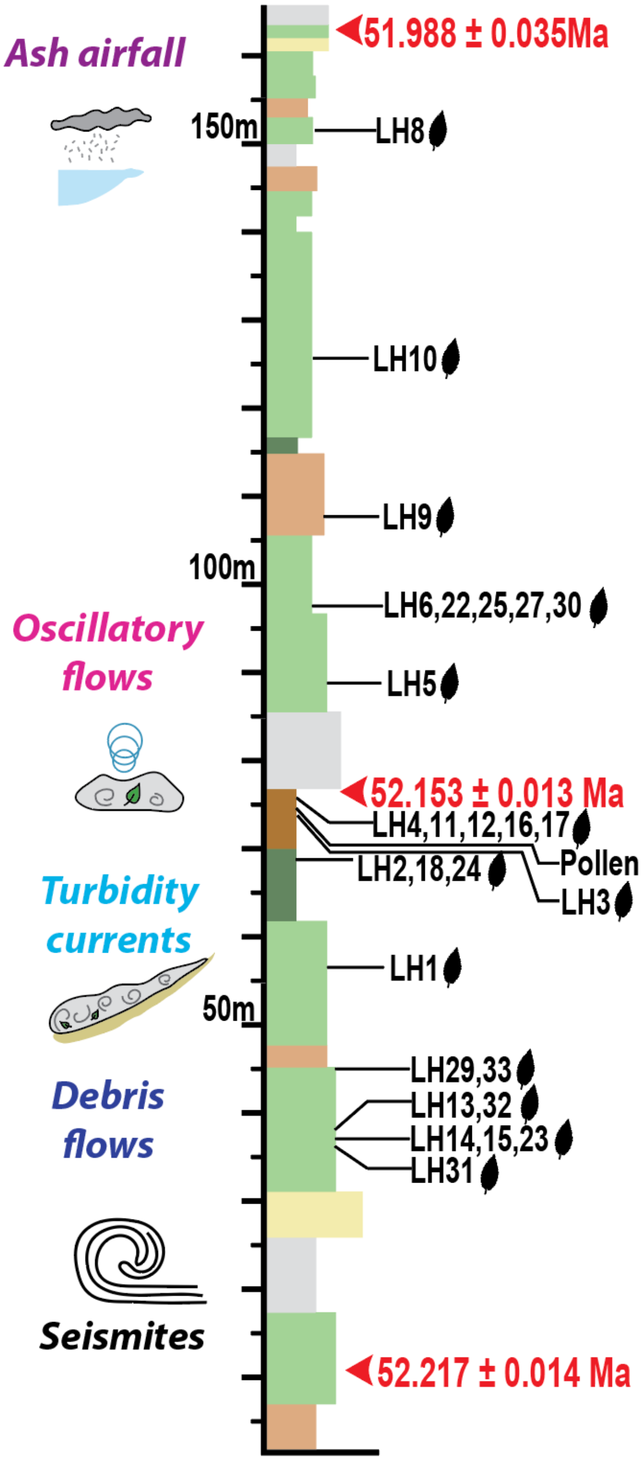

3D models of outcrop features

3D digital outcrop models were created with Agisoft Photoscan (now Metashape) software using a combination of Canon DSLR, iPhone, and DJI Phantom-acquired outcrop photos.

3D outcrop models can be explored in Sketchfab using the links below:

Overturned beds (Figure 5B)
https://sketchfab.com/3d-models/overturned-beds-laguna-del-hunco-d717f681ca0340c4bef041d502e06f1a

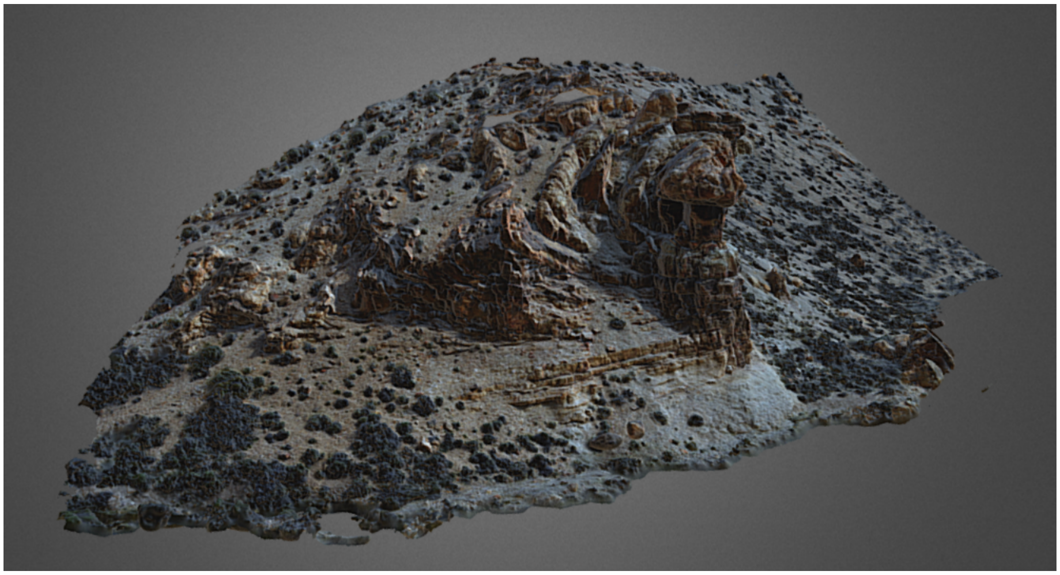

Laminated bedding and flame structures (Figure 6B)
https://sketchfab.com/3d-models/flames-7a71e7763367496598bfdcfac47fe484

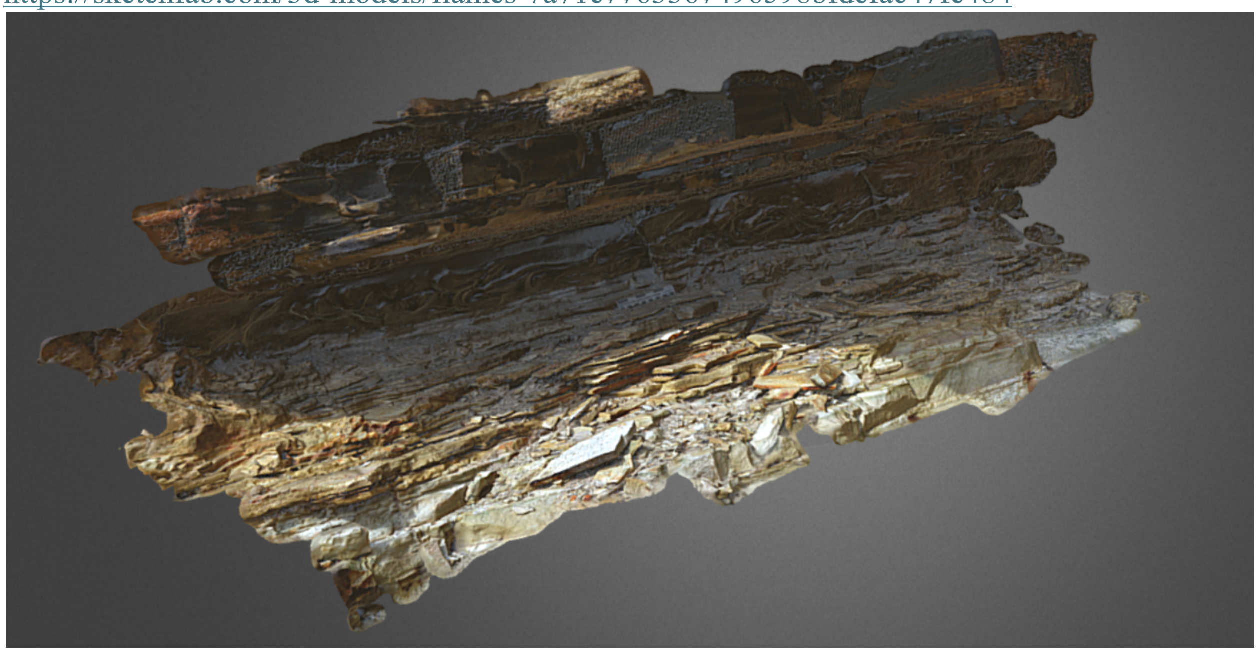

Detailed graphical log

A complete graphical sedimentology log, with detailed intervals from different facies associations, is available on the following page.

LH19-1-162
LH19-1-158
LH19-1-156
LH19-1-149
LH19-1-131
LH19-1-130
LH19-1-126
LH19-1-125
F3452-56
LH19-1-116
PLH19-1-116
F3445-51
F3440-44
LH19-1-106
F3437-39
LH19-1-102
mantecol
F3427-3
F3423-26
F3421-22
LH19-1-88
F3415-20
LH19-1-87-II
LH19-1-87-I
F3407-14
LH19-1-86
LH19-1-84
WP 1213
LH19-1-82
F3402-06
LH27
LH6
F3396-3401
LH19-1-79
F3385-91
LH19-1-77
F3392-95
LH19-1-71
F3380-84
LH19-1-65
LH19-1-61
LH19-1-59
F3378-79
F3372-77
LH19-1-55
green
white
F3368-71
F3843-53
(d/LH4 h/ S-SW)
LH19-1-53
LH19-1-52
white
WP 1212
brown
LH4
LH19-1-51
brown
green
BASE "C"
F3365-67
LH19-1-43
F3354-55
F3361-64
LH19-1-38
F3356-60
LH2
LH19-1-37
LH19-1-35
LH19-1-33
LH19-1-30
F3347-53
LH19-1-29
LH19-1-25
LH19-1-26
LH19-1-27
F3331-46
LH19-1-24
BP1705
52.024 Ma
F3326-30
F3320-25
LH19-1-19
F3318-19 (nivel 17)
F3315-17 (nivel 16)
LH19-1-14
F3312-14 (nivel 15)
LH19-1-13
F3293-3308 (niveles 13 y 14)
F3290-92
F3378-89
LH19-1-8
F3372-77
LH19-1-6
F3365-68
F3369-71
LH19-1-4
WP 1211
F3218-19
F3215-17
F3212-14
10 cm
cm lithol.
C S vf f m c vc f m c
MUD SAND GRAVEL
m lithol.